ICES REPORT 11-35

November 2011

Isogeometric Analysis of nearly incompressible large strain plasticity

by

T. Elguedj and T.J.R. Hughes

The Institute for Computational Engineering and Sciences
The University of Texas at Austin
Austin, Texas 78712

Reference: T. Elguedj and T.J.R. Hughes, "Isogeometric Analysis of nearly incompressible large strain plasticity", ICES REPORT 11-35, The Institute for Computational Engineering and Sciences, The University of Texas at Austin, November 2011.

Report Documentation Page

Form Approved
OMB No. 0704-0188

1. REPORT DATE	2. REPORT TYPE	3. DATES COVERED
NOV 2011		**00-00-2011 to 00-00-2011**

4. TITLE AND SUBTITLE	5a. CONTRACT NUMBER
Isogeometric Analysis of nearly incompressible large strain plasticity	5b. GRANT NUMBER
	5c. PROGRAM ELEMENT NUMBER
6. AUTHOR(S)	5d. PROJECT NUMBER
	5e. TASK NUMBER
	5f. WORK UNIT NUMBER
7. PERFORMING ORGANIZATION NAME(S) AND ADDRESS(ES) **University of Texas at Austin,Institute for Computational Engineering and Sciences,Austin,TX,78712**	8. PERFORMING ORGANIZATION REPORT NUMBER
9. SPONSORING/MONITORING AGENCY NAME(S) AND ADDRESS(ES)	10. SPONSOR/MONITOR'S ACRONYM(S)
	11. SPONSOR/MONITOR'S REPORT NUMBER(S)

12. DISTRIBUTION/AVAILABILITY STATEMENT
Approved for public release; distribution unlimited

13. SUPPLEMENTARY NOTES

14. ABSTRACT

We study the behavior of NURBS-based Isogeometric Analysis on problems of large-deformation plasticity. We evaluate the performance of standard NURBS elements and elements based on the F formulation of Elguedj et al. (T. Elguedj, Y. Bazilevs, V.M. Calo, T.J.R. Hughes, B and F projection methods for nearly incompressible linear and non-linear elasticity and plasticity based on higher-order NURBS elements, Com- puter Methods in Applied Mechanics and Engineering, 197 (2008), 2732{2762). We determine that standard measures of evaluation employed in the literature, namely, displacements at selected locations and graphs of reaction forces versus displacements, are often misleading. On the other hand, stress distributions, in the form of contour plots, are the most revealing measure of element performance. We also determine that the concept of mesh locking", which has dominated investigations of low-order elements, is not a relevant issue for higher-order NURBS elements for problems of large-deformation plasticity. However, standard higher-order NURBS elements of type Qk, of continuity class Ck&#56256;&#56320;1; k 2, typically exhibit spurious stress oscillations, whereas the F elements of type Qk/Qk-1 produce good results in all cases.

15. SUBJECT TERMS

16. SECURITY CLASSIFICATION OF:			17. LIMITATION OF ABSTRACT	18. NUMBER OF PAGES	19a. NAME OF RESPONSIBLE PERSON
a. REPORT **unclassified**	b. ABSTRACT **unclassified**	c. THIS PAGE **unclassified**	**Same as Report (SAR)**	**28**	

Isogeometric Analysis of nearly incompressible large strain plasticity

T. Elguedj[*,a,1], T.J.R. Hughes[b,2]

[a] *Université de Lyon, CNRS*
INSA-Lyon, LaMCoS, UMR5259
20 avenue Albert Einstein, F69621 Villeurbanne Cedex, France
[b] *Institute for Computational Engineering and Sciences, The University of Texas at Austin, 201 East 24th street, 1 University Station C0200, Austin, TX 78712-0027, USA*

Abstract

We study the behavior of NURBS-based Isogeometric Analysis on problems of large-deformation plasticity. We evaluate the performance of standard NURBS elements and elements based on the $\bar{\mathrm{F}}$ formulation of Elguedj *et al.* (T. Elguedj, Y. Bazilevs, V.M. Calo, T.J.R. Hughes, $\bar{\mathrm{B}}$ and $\bar{\mathrm{F}}$ projection methods for nearly incompressible linear and non-linear elasticity and plasticity based on higher-order NURBS elements, *Computer Methods in Applied Mechanics and Engineering*, 197 (2008), 2732–2762). We determine that standard measures of evaluation employed in the literature, namely, displacements at selected locations and graphs of reaction forces versus displacements, are often misleading. On the other hand, stress distributions, in the form of contour plots, are the most revealing measure of element performance. We also determine that the concept of "mesh locking", which has dominated investigations of low-order elements, is not a relevant issue for higher-order NURBS elements for problems of large-deformation plasticity. However, standard higher-order NURBS elements of type Qk, of continuity class $\mathcal{C}^{k-1},\ k \geq 2$, typically exhibit spurious stress oscillations, whereas the $\bar{\mathrm{F}}$ elements of type Qk/Qk-1 produce good results in all cases.

Key words: Isogeometric analysis, NURBS, multiplicative plasticity, projection method, F-bar

1. Introduction

The first applications of IsoGeometric Analysis (IGA) to nearly-incompressible elasticity problems were presented in Elguedj et al. [1] in which displacement-based $\bar{\mathrm{B}}$ and $\bar{\mathrm{F}}$ formulations for small- and large-deformation problems were developed. These methods employed a lower-order space for representing volumetric deformations in order to avoid mesh locking due to nearly isochoric kinematics. The $\bar{\mathrm{B}}$ formulation developed was standard, following the original ideas of Hughes [2, 3]. However, the $\bar{\mathrm{F}}$ formulation was novel and, in our opinion, was an improvement over what had existed previously. The basis of its derivation was a modified minimum potential energy principle, the modification being the representation of the deformation gradient in terms of an "improved" $\bar{\mathrm{F}}$. The consistent tangent stiffness matrix was shown to be symmetric and contained several "unexpected terms" (see Elguedj et al. [1] for further details). When combined with a Newton-Raphson solution strategy, it exhibited second-order iterative convergence, as theoretically predicted. The selection of the spaces of basis functions was based on the desire to include and generalize the most utilized finite elements for nonlinear solid mechanics computations, namely, the four-node quadrilateral and eight-node hexahedral, "constant pressure elements", which have been the stalwarts of nonlinear commercial and research codes for approximately 40 years. The basis functions may be described as "Qk/Qk-1" that is, the displacement are denoted Qk, and are $\mathcal{C}^{k-1}$-continuous, whereas the volumetric measures of strain, namely, the dilatation in the small-deformation case, and the jacobian of the deformation gradient in the large-deformation case, are denoted Qk-1 and are $\mathcal{C}^{k-2}$-continuous.

[*] Corresponding author
Email address: thomas.elguedj@insa-lyon.fr (T. Elguedj)
[1] Assistant Professor
[2] Professor of Aerospace Engineering and Engineering Mechanics, Computational and Applied Mathematics Chair III

Clearly, when $k = 1$ this reduces to our version of the constant pressure element, that is, Q1/Q0. The higher-order and smooth versions of these elements, for which $k \geq 2$, were previously unexplored, but were shown to perform very effectively on a number of test cases. However, the "standard" higher-order NURBS elements of type Qk, $k \geq 2$, produced poor displacements and especially poor stresses, whereas the $\bar{\mathrm{B}}$ and $\bar{\mathrm{F}}$ elements produced accurate displacements *and* stresses in all cases. An initial application to a problem of plasticity was presented but the subject was not systematically pursued.

The present paper picks up where Elguedj et al. [1] left off and investigates the behavior of higher-order NURBS elements on problems of large-deformation elastoplasticity. We utilize a hyperelastic-based elastoplastic theory, presented in Simo and Hughes [4], that has been employed in many investigations of numerical methods. The theory is based on the now classical $\mathbf{F} = \mathbf{F}^e\mathbf{F}^p$ multiplicative split of the deformation gradient into elastic and plastic parts. The deformation gradient used in the numerics is the $\bar{\mathrm{F}}$ mentioned previously. Based on numerical studies of benchmark problems, our experiences in large-deformation elastoplasticity are somewhat different than those for nonlinear elasticity. Displacements for standard higher-order NURBS elements are sometimes as good as for $\bar{\mathrm{F}}$ elements. However, stresses are a much more discerning measure. Stresses are very good for the $\bar{\mathrm{F}}$ elements but, typically, very bad for the standard elements. Stresses invariably are the critical differentiating measure in problems of large-deformation plasticity.

An outline of the paper follows: in Section 2 we very briefly introduce some ideas from NURBS-based IGA. For more extensive treatments we recommend Hughes et al. [5], Cottrell et al. [6] and, in particular, Elguedj et al. [1], in which many results pertinent to this work are presented. The $\mathbf{F} = \mathbf{F}^e\mathbf{F}^p$ formulation of plasticity is briefly reviewed in Section 3 and the strain energy function, Mises-Huber yield surface, nonlinear isotropic hardening law, and associative flow rule are defined. The $\bar{\mathrm{F}}$ method is also described in Section 3, along with the constitutive algorithm and consistent elastoplastic moduli. Numerical examples are presented in Section 4. The evaluations of the procedures and comparisons with the Q1/P0 element results of Simo and Armero [7], the mixed method elements of Taylor [8], and the standard NURBS elements (*i.e.*, those not using the $\bar{\mathrm{F}}$ methodology), are the main contributions of this paper. Several themes emerge:

1. As indicated previously, displacements can be very misleading for higher-order elements. In particular, the idea that larger displacements are better does not hold up under scrutiny. Standard higher-order NURBS elements of type Qk do *not* lock and often produce displacements as large as those for corresponding $\bar{\mathrm{F}}$ elements, but their stress distributions are invariably oscillatory, revealing serious defects.
2. Plots of reaction forces versus displacements can also be misleading.
3. Contour plots of stresses immediately reveal problems with element formulations, as will be evident from the results presented in the sequel.
4. It is important to study refined finite element meshes because ill-conceived elements may produce results on refined meshes that are no better than for coarse meshes. Obviously, the opposite holds true for well-conceived elements. We note that most studies presented in the literature heretofore only present solutions on very coarse meshes.

Our conclusions and our suggestions for further research are presented in Section 5.

2. NURBS-based isogeometric analysis

2.1. Basics

We briefly review the concept of NURBS-based IGA first presented in Hughes et al. [5], Cottrell et al. [6], where a detailed account may be found. NURBS are a generalization of B-splines and standard in CAD and computer graphics for geometry modeling (see, *e.g.*, Cohen et al. [9], Piegl and Tiller [10], Farin [11]).

B-splines are piecewise polynomial functions with a prescribed degree of continuity. Univariate B-spline basis functions are constructed from a knot vector, a set of coordinates in parametric space, $\Xi = \{\xi_1, \xi_2, \ldots, \xi_{n+p+1}\}$, where $\xi_i \in \mathbb{R}$ is the i^{th} knot, i is the knot index, $i = 1, 2, \ldots, n + p + 1$, p is the polynomial order, and n is the number of basis functions. More than one knot can be placed at the same location in the parametric space. If m is the multiplicity of a given knot, the functions are C^{p-m} continuous at that location. If the knots are equally spaced, the knot vector is said to be uniform. A

knot vector is referred to as open if its first and last knots have multiplicity $p+1$. This results in the basis being interpolatory at the endpoints of the interval.

B-spline basis functions for a given order p, are defined recursively in the parametric space by way of the knot vector Ξ. Beginning with piecewise constants ($p = 0$) we have

$$N_{i,0}(\xi) = \begin{cases} 1 & \text{if } \xi_i \leq \xi < \xi_{i+1}, \\ 0 & \text{otherwise.} \end{cases} \tag{1}$$

For $p = 1, 2, 3, \ldots$, the basis is defined by the Cox-de Boor recursion formula (see, *e.g.*, Cohen et al. [9]):

$$N_{i,p}(\xi) = \frac{\xi - \xi_i}{\xi_{i+p} - \xi_i} N_{i,p-1}(\xi) + \frac{\xi_{i+p+1} - \xi}{\xi_{i+p+1} - \xi_{i+1}} N_{i+1,p-1}(\xi). \tag{2}$$

Let d_s denote the number of spatial dimensions. A B-spline curve in $\mathbb{R}^{d_s}$ is defined as follows:

$$\mathbf{C}(\xi) = \sum_{i=1}^{n} \mathbf{P}_i N_{i,p}(\xi), \tag{3}$$

where $\mathbf{P}_i \in \mathbb{R}^{d_s}$ denotes control point i.

The univariate B-spline concept can be extended to multiple dimensions with the use of tensor products, but representation of many desired shapes of engineering interests, such as conic sections, require further generalization. Non-Uniform Rational B-Splines (NURBS), rational projections of higher dimensional B-splines, can be introduced for this purpose and consequently share many of the same properties as B-splines. More details can be found in Cohen et al. [9], Rogers [12] and Piegl and Tiller [10], as well as Cottrell et al. [6].

2.2. k-refinement

Analogues of finite element h-and p-refinement are available in IGA. h-refinement is termed knot insertion and consists in adding new knots in the knot vectors. Knot insertion does not change the geometric modeling and preserves continuity as long as new knots are not already present in the knot vector. p-refinement is termed order elevation and consists in increasing the polynomial order of the basis functions. As with knot insertion, neither the geometry nor the parametrization is changed during the process. Moreover, continuity is preserved at element boundaries by increasing knot multiplicity. The main difference in IGA when comparing refinement strategies with finite element ones is that h-and p-refinement do not commute. The flexibility of knot insertion and order elevation allows us to introduce k-refinement in which order and continuity of the basis functions can be simultaneously increased. This can be attained by performing order elevation on the coarse geometric mesh followed by knot insertion up to the desired mesh refinement. It is important to note that k-refinement will produce maximum continuity on a patch if the coarsest mesh is comprised of a single element. If the initial mesh comprises constraints on continuity across element boundaries, these will exist on all meshes. For more insight on mesh generation and refinement in IGA see Cottrell et al. [6, Chapter 2].

3. Nearly incompressible nonlinear elasticity and plasticity

3.1. Elastoplasticity at finite strains

In this section, we briefly review the basics of elastoplastic constitutive models at finite strains based on the notion of an intermediate stress free configuration. More details can be found for example in Simo [13, 14] and Simo and Hughes [4, Chapter 9].

3.1.1. Kinematic preliminaries

Let $\mathcal{B} \subset \mathbb{R}^3$ be the reference configuration of a body and $\mathcal{B}' \subset \mathbb{R}^3$ be its deformed configuration. We introduce a mapping $\boldsymbol{\phi} : \mathcal{B} \to \mathcal{B}'$, the deformation, that takes a point $\mathbf{X} \in \mathcal{B}$ to a point $\mathbf{x} = \boldsymbol{\phi}(\mathbf{X}) \in \mathcal{B}'$. The deformation gradient is the second-order tensor defined by

$$\mathbf{F} = \nabla^X \phi(\mathbf{X}) = \frac{\partial \boldsymbol{\phi}(\mathbf{X})}{\partial \mathbf{X}}. \tag{4}$$

The considered formulation is based on two hypotheses:

1. The introduction of an intermediate local configuration, relative to which the elastic response is characterized, which leads to a multiplicative decomposition of the deformation gradient:
$$\mathbf{F} = \mathbf{F}^e \mathbf{F}^p. \tag{5}$$
2. The principle of maximum plastic dissipation.

Following Eq. (5), we can introduce elastic Eulerian tensors and plastic Lagrangian ones as:

$$\mathbf{b}^e = \mathbf{F}^e\mathbf{F}^{eT} \text{ and } \mathbf{e}^e = \frac{1}{2}(\mathbf{1} - (\mathbf{b}^e)^{-1}), \quad (6)$$

$$\mathbf{C}^p = \mathbf{F}^{pT}\mathbf{F}^p \text{ and } \mathbf{E}^p = \frac{1}{2}(\mathbf{C}^p - \mathbf{1}). \quad (7)$$

Using the previous equations, we can write:

$$\mathbf{b}^e = \mathbf{F}\mathbf{C}^{p-1}\mathbf{F}^T. \quad (8)$$

Using the definition of the total rate of deformation tensor, we can express the total rate of the elastic left Cauchy Green tensor as a Lie derivative by the following equation:

$$\begin{aligned} L_v\mathbf{b}^e &= \mathbf{F}\left\{\frac{\partial}{\partial t}\mathbf{F}^{-1}\mathbf{b}^e\mathbf{F}^{-T}\right\}\mathbf{F}^T \\ &= \mathbf{F}\dot{\mathbf{C}}^{p-1}\mathbf{F}^T. \end{aligned} \quad (9)$$

Within the context of the infinitesimal theory, the small strain tensor $\boldsymbol{\varepsilon}$ is decomposed into volumetric and deviatoric parts using an additive split. In the nonlinear theory, the decomposition becomes multiplicative:

$$\mathbf{F} = \mathbf{F}^{\text{dil}}\mathbf{F}^{\text{dev}}, \quad (10)$$

where

$$\text{det}\mathbf{F} = J = \text{det}\mathbf{F}^{\text{dil}} \text{ and } \text{det}\mathbf{F}^{\text{dev}} = 1, \quad (11)$$

which leads to:

$$\mathbf{F}^{\text{dev}} = J^{-1/3}\mathbf{F} \text{ and } \mathbf{F}^{\text{dil}} = J^{1/3}\mathbf{I}. \quad (12)$$

3.1.2. J_2 flow theory at finite strains

We consider a J_2 flow theory with isotropic hardening. We assume that the stress response is isotropic and that the plastic flow is isochoric, that is:

$$\begin{aligned} &\text{det}\mathbf{F}^p = \text{det}\mathbf{C}^p = 1 \quad \text{and} \\ &J = \text{det}\mathbf{F} = \text{det}\mathbf{F}^e. \end{aligned} \quad (13)$$

Using the assumption of isotropy and the intermediate stress free configuration, the stress response can be characterized using a nonlinear elastic strain energy function:

$$\begin{aligned} &W = U(J^e) + \bar{W}(\bar{\mathbf{b}}^e), \quad \text{with} \\ &\bar{\mathbf{b}}^e = (J^e)^{-2/3}\mathbf{b}^e. \end{aligned} \quad (14)$$

In the remaining, we will use the following expressions for the isochoric and volumetric parts of the strain energy function:

$$U(J) = \frac{1}{2}\kappa\left(\frac{1}{2}(J^2 - 1) - \ln J\right), \quad (15)$$

$$\bar{W}(\bar{\mathbf{b}}) = \frac{1}{2}\mu\left(\text{tr}[\bar{\mathbf{b}}] - 3\right), \quad (16)$$

where κ is interpreted as the bulk modulus and μ the shear modulus in infinitesimal deformations.

We consider the classical Mises-Huber yield condition, formulated in terms of the Kirchhoff stress tensor as:

$$f(\boldsymbol{\tau}, \alpha) = \|\text{dev}[\boldsymbol{\tau}]\| - \sqrt{\frac{2}{3}}k(\alpha) \leq 0. \quad (17)$$

We will consider in this paper a nonlinear isotropic hardening law using the following expression (see, *e.g.*, Simo and Hughes [4]):

$$\begin{aligned} k(\alpha) = \sigma_0 &+ (\sigma_\infty - \sigma_0)[1 - \exp(-\delta\alpha)] \\ &+ K\alpha, \quad \text{with} \quad \delta > 0, \end{aligned} \quad (18)$$

where σ_0 is the initial flow stress, σ_∞ is the saturation flow stress, δ is the saturation exponent, K is the linear hardening coefficient, and α is the equivalent plastic strain.

As in the infinitesimal theory, the associative flow rule is uniquely determined by the principle of maximum plastic dissipation given the strain energy function and the yield condition:

$$L_v\mathbf{b}^e = -\frac{2}{3}\gamma\text{tr}[\mathbf{b}^e]\mathbf{n}, \quad (19)$$

$$\mathbf{n} = \mathbf{s}/\|\mathbf{s}\|, \quad (20)$$

$$\mathbf{s} = \text{dev}[\boldsymbol{\tau}]. \quad (21)$$

The evolution of the hardening variable is the same as in the infinitesimal theory:

$$\dot{\alpha} = \sqrt{\frac{2}{3}}\gamma, \quad (22)$$

where γ is the consistency parameter subject to the Kuhn-Tucker conditions:

$$\gamma \geq 0, \quad f(\boldsymbol{\tau}, \alpha) \leq 0, \quad \gamma f(\boldsymbol{\tau}, \alpha) = 0, \quad (23)$$

with the consistency condition

$$\gamma\dot{f}(\boldsymbol{\tau}, \alpha) = 0. \quad (24)$$

3.1.3. Integration algorithm

The integration algorithm of the previous formulation can be obtained using the general procedure presented in Simo and Hughes [4]. We proceed as follows:

- The equations are pull-backed to the material description using the deformation gradient.
- The time stepping algorithm is performed in the material description. In our case we use backward Euler.
- The discrete evolution equations are pushed forward to the spatial description using the deformation gradient.

Using the obtained equations, the return mapping algorithm can be constructed, the problem being strain driven. This algorithm is summarized in Box 1. In addition, we present in the appendix the expression for the consistent elastoplastic moduli for the proposed radial return algorithm (see Simo [13, 14]) as well as the iterative algorithm used to solve the consistency condition for the proposed nonlinear isotropic hardening law.

3.2. $\bar{F}$ formulation for nearly incompressible nonlinear elasticity and plasticity

The $\bar{\mathrm{F}}$ method is a generalization of the $\bar{\mathrm{B}}$ method (see, *e.g.*, Hughes [2, 3]), a strain-projection technique, to the hyperelastic finite-deformation regime. The central idea is to multiplicatively split the deformation gradient tensor $\mathbf{F}$ into its deviatoric (volume preserving) and dilatational (volume changing) parts as given in Eq. (10). This decomposition has been exploited previously by Flory [15], Hughes et al. [16], Simo et al. [17], Simo and Taylor [18] (within a three field Hu-Washizu principle), and, more recently, de Souza Neto et al. [19, 20] in an alternative $\bar{\mathrm{F}}$ approach.

We define a modified deformation gradient $\bar{\mathbf{F}}$ in terms of $\mathbf{F}^{\mathrm{dev}}$ and a modified dilatational part of the deformation gradient $\bar{\mathbf{F}}^{\mathrm{dil}}$:

$$\bar{\mathbf{F}} = \bar{\mathbf{F}}^{\mathrm{dil}}\mathbf{F}^{\mathrm{dev}}, \tag{25}$$

where

$$\bar{\mathbf{F}}^{\mathrm{dil}} = \overline{\mathbb{P}}(\mathbf{F}^{\mathrm{dil}}) = \overline{\mathbb{P}}(J^{1/3})\mathbf{I} = \overline{J^{1/3}}\mathbf{I}, \tag{26}$$

with $\overline{\mathbb{P}}$ a linear projection operator with respect to the L^2-norm onto a space of lower-order and lower-continuity functions. This allows us to obtain a robust formulation with only displacements as primary unknowns in order to solve large strain nearly incompressible problems. For piecewise polynomial basis functions such as NURBS, the projection space is taken as the space one order lower than the displacement space. This introduces the family of elements Qk/Qk-1 where k is the polynomial order of the displacement space. The space Qk is $\mathcal{C}^{k-1}-$continuous and the space Qk-1 is $\mathcal{C}^{k-2}-$continuous. For further details the interested reader should refer to Elguedj et al. [1].

We employ here the proposed $\bar{\mathrm{F}}$ method in conjunction with the previously presented elastoplastic model. In practice this comes down to using the modified deformation gradient $\bar{\mathbf{F}}$ instead of the original deformation gradient $\mathbf{F}$ as an input in all the elastoplastic routines. The internal force vector and consistent tangent stiffness matrix for hyperelasticity are defined in Elguedj et al. [1]. For the elastoplastic theory used here, we construct the consistent tangent stiffness matrix by replacing the tensor of elastic moduli in the formula derived in Elguedj et al. [1] by the elastic-plastic moduli presented in Box 2.

4. Examples

In all the examples presented in the following subsections, the material model consists of a Neo-Hookean one for the elastic part, and an associative flow rule based on a Von Mises yield criterion with nonlinear isotropic hardening following a saturation law for the plastic part. The nonlinear isotropic hardening rule is defined from Eqs. (17) and (18). The strain energy function of the Neo-Hookean model is given by Eqs. (15) and (16). The same material parameters are used in all the examples and are given in Table 1.

Shear modulus μ	80.1938 GPa
Bulk modulus κ	164.21 GPa
Initial flow stress σ_0	450 MPa
Saturation flow stress σ_∞	715 MPa
Saturation exponent δ	16.93
Linear hardening coefficient K	129.24 MPa

Table 1: Elastic-plastic material properties.

4.1. Cook's membrane

We consider as a first example the elastic-plastic extension of the well known Cook's membrane.

1. Update current configuration

$$\boldsymbol{\phi}_{n+1} = \boldsymbol{\phi}_n + \mathbf{u}_n \circ \boldsymbol{\phi}_n = \boldsymbol{\phi}_n(\mathbf{X}) + \mathbf{u}_n[\boldsymbol{\phi}_n(\mathbf{X})],$$
$$\mathbf{f}_{n+1} = \mathbf{1} + \tfrac{\partial \mathbf{u}_n}{\partial \mathbf{x}_n},$$
$$\mathbf{F}_{n+1} = \mathbf{f}_{n+1}\mathbf{F}_n.$$

2. Compute elastic predictor

$$\bar{\mathbf{f}}_{n+1} = (\det[\mathbf{f}_{n+1}])^{-1/3}\,\mathbf{f}_{n+1},$$
$$\bar{\mathbf{b}}^{e\ trial}_{n+1} = \bar{\mathbf{f}}_{n+1}\bar{\mathbf{b}}^{e}_{n}\bar{\mathbf{f}}^{T}_{n+1},$$
$$\mathbf{s}^{trial}_{n+1} = \mu \mathrm{dev}[\bar{\mathbf{b}}^{e\ trial}_{n+1}].$$

3. Check for plastic loading

Compute $f^{trial}_{n+1} = \|\mathbf{s}^{trial}_{n+1}\| - \sqrt{\tfrac{2}{3}}K(\alpha_n)$.

if $f^{trial}_{n+1} \leq 0$ *then* elastic state $\Rightarrow$ save and exit,

else perform return mapping.

4. Return mapping

$$\bar{\mu} = \tfrac{1}{3}\mu \mathrm{tr}[\bar{\mathbf{b}}^{e\ trial}_{n+1}]\ ,$$

Compute $\Delta\gamma$ such that $\hat{f}(\Delta\gamma) = \|\mathbf{s}^{trial}_{n+1}\| - \sqrt{\tfrac{2}{3}}K(\alpha_n + \tfrac{2}{3}\Delta\gamma) - 2\bar{\mu}\Delta\gamma = 0,$

$$\mathbf{n} = \mathbf{s}^{trial}_{n+1}/\|\mathbf{s}^{trial}_{n+1}\|\ ,$$
$$\mathbf{s}_{n+1} = \mathbf{s}^{trial}_{n+1} - 2\bar{\mu}\Delta\gamma\mathbf{n}\ ,$$
$$\alpha_{n+1} = \alpha_n + \sqrt{\tfrac{2}{3}}\Delta\gamma\ .$$

5. Stress update

$$J_{n+1} = \det[\mathbf{F}_{n+1}] \Rightarrow p_{n+1} = U'(J_{n+1}) = \tfrac{\kappa}{2}(J^2_{n+1} - 1)/J_{n+1},$$
$$\boldsymbol{\tau}_{n+1} = J_{n+1}p_{n+1}\mathbf{1} + \mathbf{s}_{n+1}.$$

6. Update intermediate configuration

$$\bar{\mathbf{b}}^{e}_{n+1} = (1/\mu)\mathbf{s}_{n+1} + (\bar{\mu}/\mu)\mathbf{1}.$$

Box 1: Return-mapping algorithm for J_2-flow theory with nonlinear isotropic hardening.

This example has been studied by many researchers to validate new methods to treat incompressibility under combined bending and shear in both small and large deformation cases. The extension to large strain plasticity was proposed by Simo and Armero [7] and later studied by Armero and Glaser [21] and Ramesh and Maniatty [22]. A tapered panel is clamped on one side and subjected to a uniform vertical shear load on the opposite side. The other sides are traction free. The geometry, loading and boundary conditions are given in Figure 1. The load value is chosen to be $F = 5N/mm$ and is imposed in ten equal steps. Plain strain conditions are assumed to apply.

The results, shown in Figure 2 for the vertical displacement of the top right point versus number of elements per side, compare well to those obtained in Simo and Armero [7] and Armero and Glaser [21]. Similar convergence behavior, when increasing the order of approximation with the proposed $\bar{\mathrm{F}}$ method, to those obtained in the nearly incompressible linear and nonlinear elastic cases (see Elguedj et al. [1]) is obtained. In Figure 3, we show the σ_{yy} component of the Cauchy stress tensor for the 4×4 element mesh with linear, quadratic and cubic NURBS with and without $\bar{\mathrm{F}}$. We can see stress oscillation patterns for the non-$\bar{\mathrm{F}}$ cases, even for the cubic NURBS that showed reasonable convergence for the top right corner displacement. This behavior is also similar to what was observed by

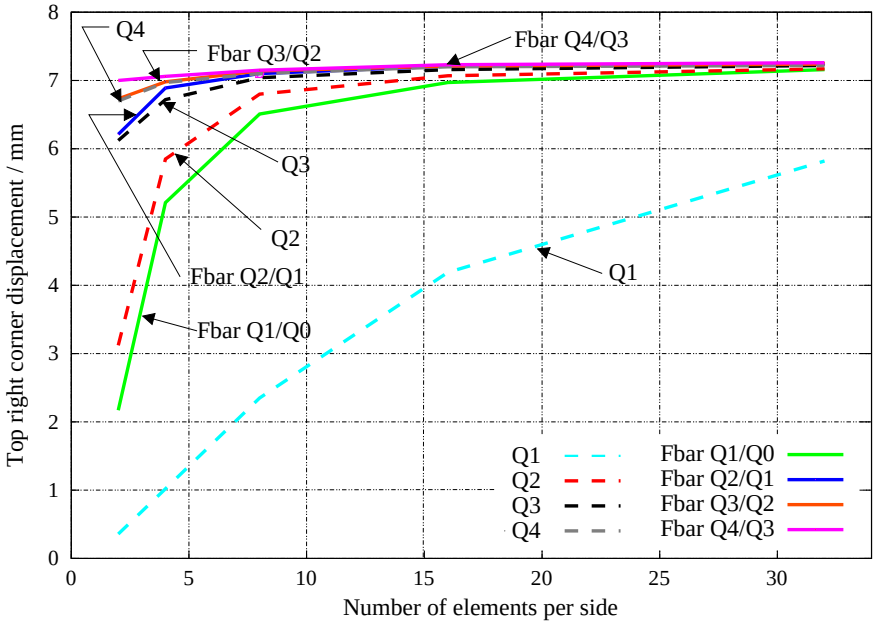

Figure 2: Elastic-plastic Cook's membrane. Vertical displacement of top right corner versus number of elements per edge with and without $\bar{\mathrm{F}}$ for various NURBS orders obtained from k-refinement.

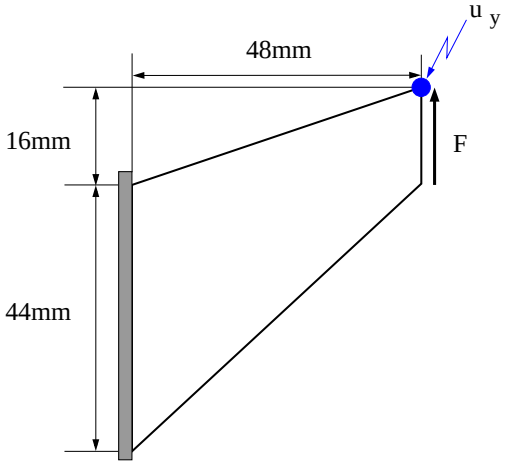

Figure 1: Geometry, loading, boundary conditions, material parameters and quantity of interest for the plane strain Cook's membrane.

the authors in the nonlinear elastic incompressible case in [1]. Clear locking behavior may be noted for Q1 in Figure 2, but not Q2 and Q3. However, stress oscillations which are especially apparent for Q2, are initial indications of deficiencies of non-$\bar{\mathrm{F}}$ elements.

4.2. Plane strain necking of a bar

In the second example, we consider a plane-strain bar subjected to uniform extension. This is a standard test problem that was also analyzed by Simo and Armero [7], Armero and Glaser [21], Dvorkin and Assanelli [23], de Souza Neto et al. [19, 20], agelet de Saracibar et al. [24] and Taylor [8]. The bar has a length of 53.334mm and a width of 12.826mm, symmetry conditions are used and only one fourth of the domain is modeled in the numerical simulation as presented in Figure 4. In order to control the location of the necking, the dimension at the center of the bar is reduced to 0.982 of the top width. A total displacement of 5mm is applied on the top surface. Numerical simulations are performed with meshes of 50 and 200 elements with refinement near the necking area (see Figure 4).

In Figures 5 and 6 we plot the σ_{yy} component of the Cauchy stress tensor and the equivalent plastic strain on the deformed configuration at maximum load for linear, quadratic and cubic cases with and

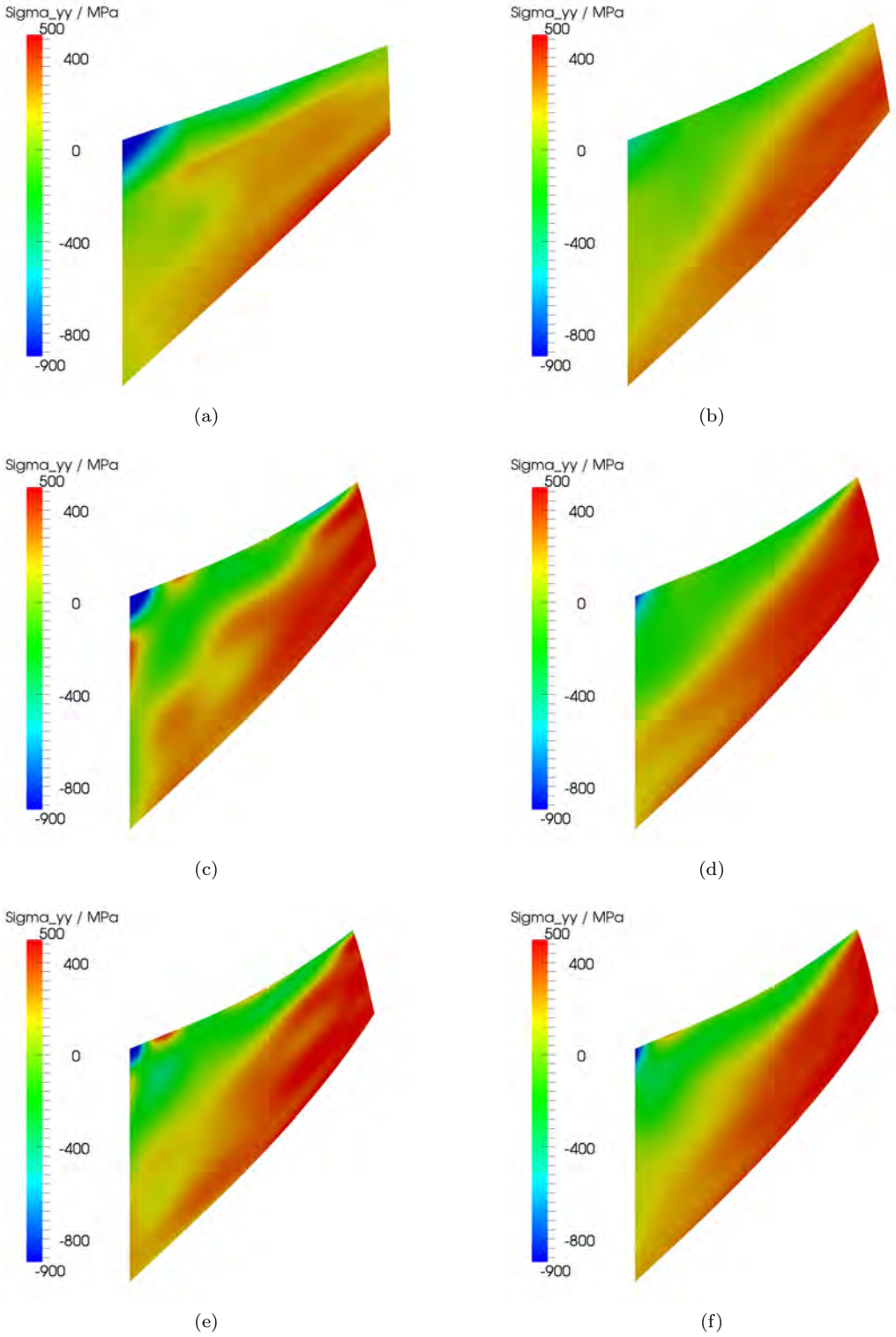

Figure 3: Elastic-plastic Cook's membrane, coarse mesh with four elements per side. σ_{yy} Cauchy stress component at maximum load for (a) Q1, (c) Q2, (e) Q3, (b), $\bar{\mathrm{F}}$ Q1/Q0 (d) $\bar{\mathrm{F}}$ Q2/Q1 (f) $\bar{\mathrm{F}}$ Q3/Q2.

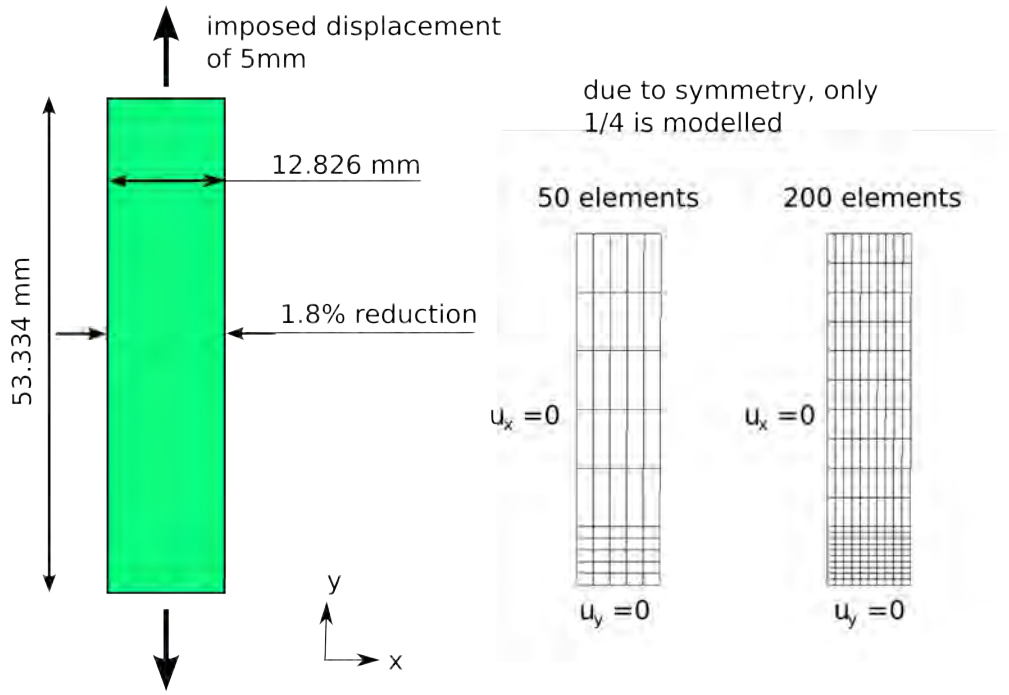

Figure 4: Plane strain necking: problem setup and quarter meshes used for the computation

without $\bar{\mathrm{F}}$ for the 50 element case. All results are shown with different scales adapted to the minimum and maximum values obtained in each case. For the non-$\bar{\mathrm{F}}$ cases, we can clearly see oscillation patterns due to locking for the stress. Such patterns cannot be seen in the $\bar{\mathrm{F}}$ cases even for the linear case with this relatively coarse mesh. Although we observe stress oscillations, the deformed shapes of the specimen look very similar between the $\bar{\mathrm{F}}$ and non-$\bar{\mathrm{F}}$ cases for quadratic and cubic functions. From Figure 5 we observe that the minimum and maximum values of the σ_{yy} component of the Cauchy stress tensor for the piecewise linear case are every different from the values for the quadratic and cubic cases, for both the $\bar{\mathrm{F}}$ and non-$\bar{\mathrm{F}}$ cases. These values are quite close to each other when quadratic and cubic $\bar{\mathrm{F}}$ cases are compared. Similar observations can be made for the equivalent plastic strain in Figure 6.

In Figures 7 and 8 we plot the horizontal displacement at the bottom right corner of the specimen (*i.e.*, where necking occurs) and the reaction force versus the imposed vertical displacement. Results are plotted with dashed lines for non-$\bar{\mathrm{F}}$ cases and solid lines for $\bar{\mathrm{F}}$ cases. We can see that $\bar{\mathrm{F}}$ Q1/Q0 provides reasonable results but that the mesh is too coarse to achieve the results of Q2/Q1 and Q3/Q2. As for the Cook's membrane we can note that for the non-$\bar{\mathrm{F}}$ Q2 and Q3 cases, although stress oscillations are observed, global parameters such as displacement and reaction force are close to the correct values.

In Figures 9 to 12 we plot similar results as previously but for the 200 element case. All results are shown with different scales adapted to the minimum and maximum values obtained in each case. We can still observe oscillations for the stress in the non-$\bar{\mathrm{F}}$ cases. As with the coarse mesh, the minimum and maximum values for both quantities for the Q1 case are very different from the other cases. However, we can see that for Q1/Q0 the maximum and minimum values are converging to the ones obtained in the Q2/Q1 and Q3/Q2 cases. For the necking displacement and the reaction force, we also plotted results obtained using mixed finite elements Q1/P0 and Q2/P1 quadrilaterals taken from Taylor [8]. We can see that the results for Q1/P0 are identical to the ones obtained with Q1/Q0 and that results for Q2/P1 are very close to Q2/Q1. We note that the results for $\bar{\mathrm{F}}$ Q3/Q2 and Q2/Q1 are indistinguishable (results are identical up to the fifth digit for both quantities). We also wish to emphasize that, in our opinion, the necking displacement and reaction results may be misleading in that even when

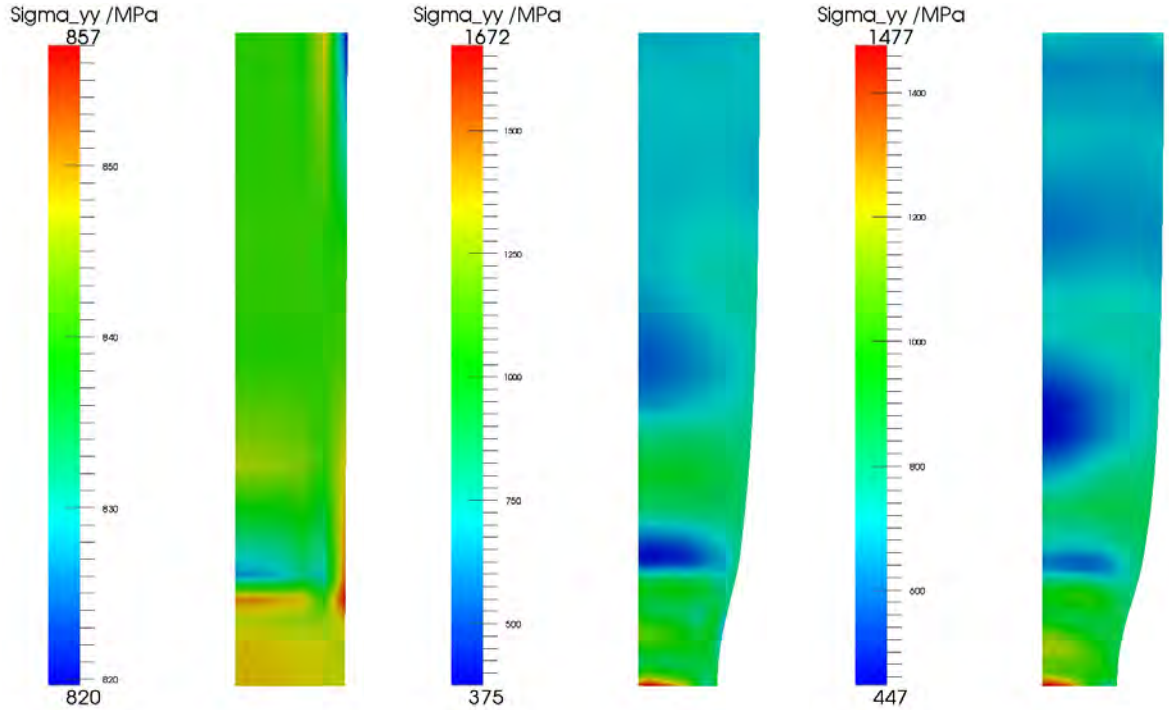

Figure 5: Plane strain necking, coarse mesh with 50 elements. σ_{yy} Cauchy stress component for a vertical imposed displacement of 5mm for: (a) Q1, (b) Q2, (c) Q3, (d) $\bar{\mathrm{F}}$ Q1/Q0, (e) $\bar{\mathrm{F}}$ Q2/Q1, (f) $\bar{\mathrm{F}}$ Q3/Q2.

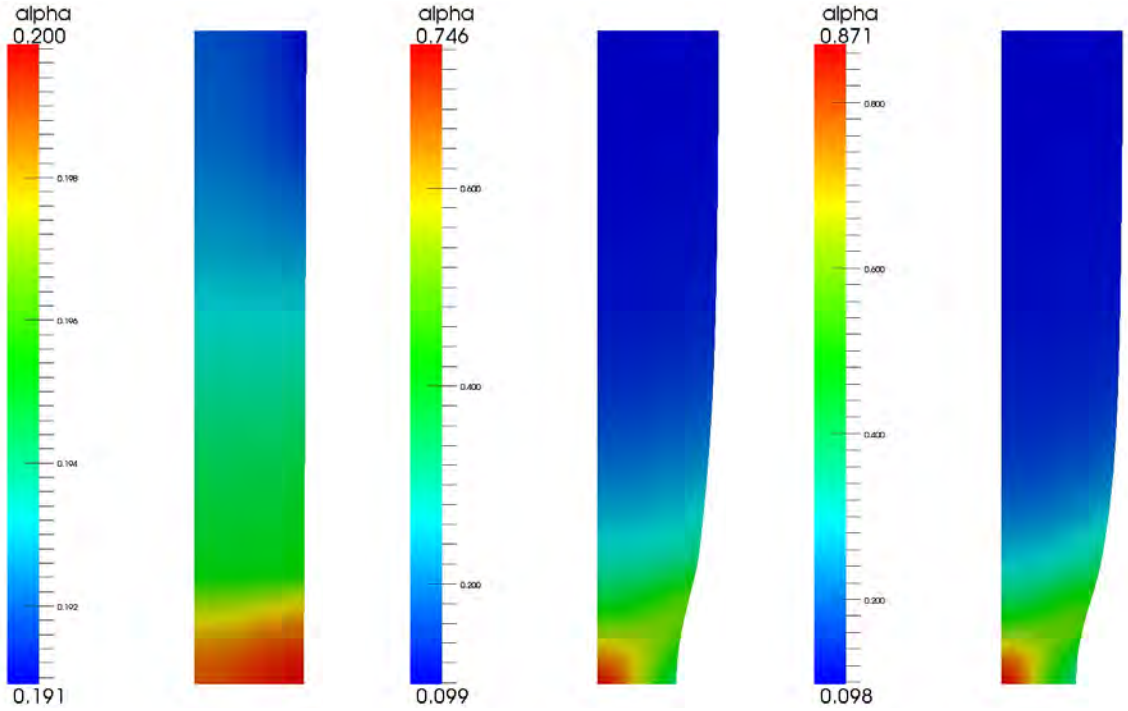

(a) (b) (c)

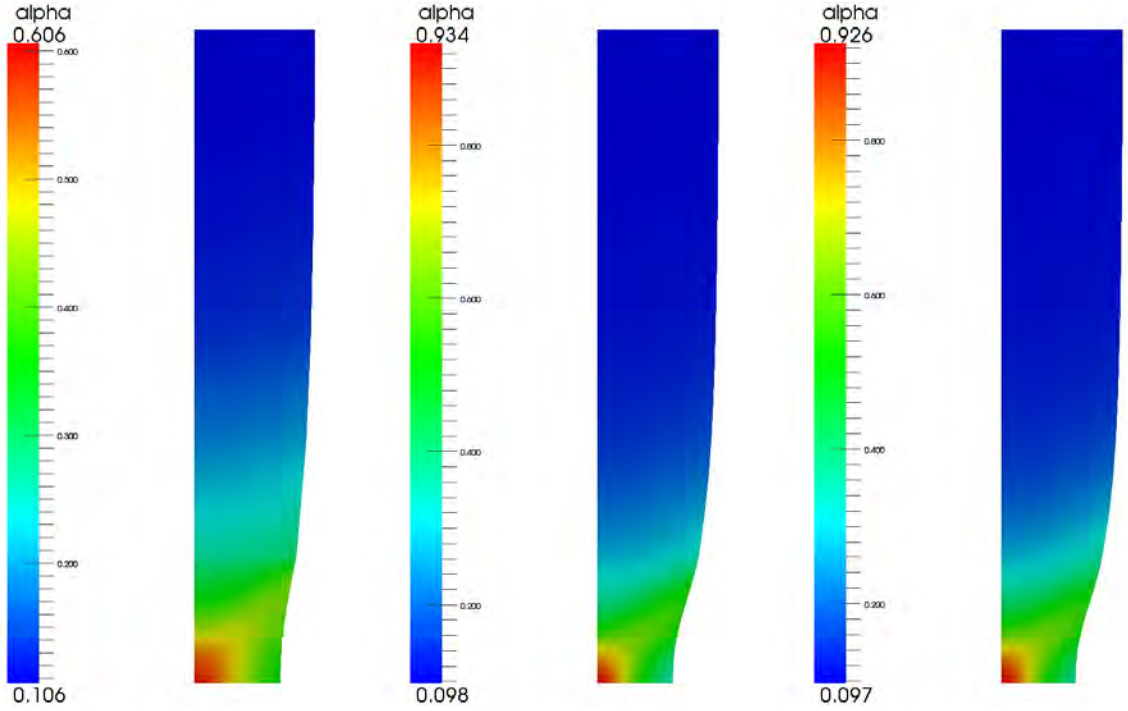

(d) (e) (f)

Figure 6: Plane strain necking, coarse mesh with 50 elements. Equivalent plastic strain α for a vertical imposed displacement of 5mm for: (a) Q1, (b) Q2, (c) Q3, (d) $\bar{\mathrm{F}}$ Q1/Q0, (e) $\bar{\mathrm{F}}$ Q2/Q1, (f) $\bar{\mathrm{F}}$ Q3/Q2.

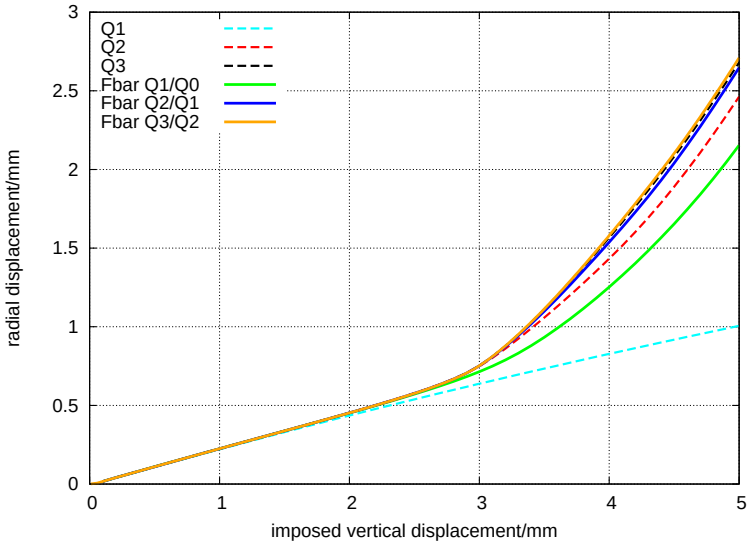

Figure 7: Plane strain necking, coarse mesh with 50 elements. Necking displacement versus imposed displacement.

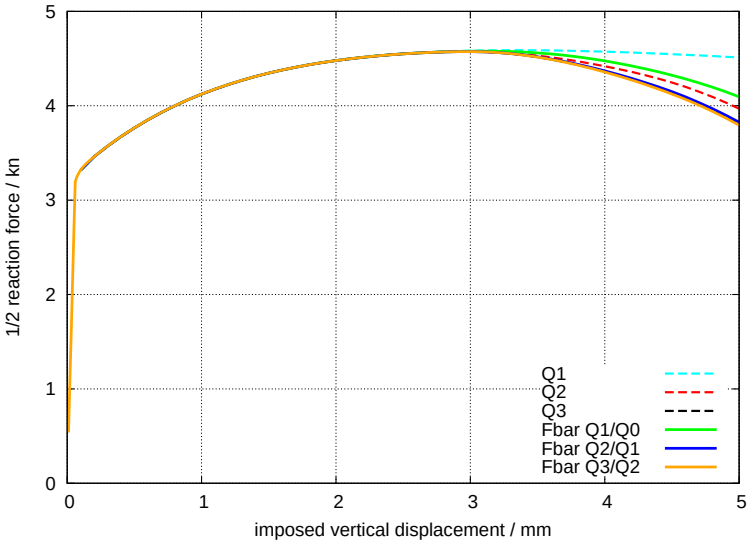

Figure 8: Plane strain necking, coarse mesh with 50 elements. Half reaction force versus imposed displacement.

stresses are clearly inaccurate, such as for the cases Q2 and Q3, the necking and reaction results are very similar to those for $\bar{\text{F}}$ Q2/Q1 and $\bar{\text{F}}$ Q3/Q2.

4.3. Three dimensional necking

The final example is the three-dimensional extension of the previous one. It has been studied by Simo and Armero [7], de Souza Neto et al. [19, 20] and agelet de Saracibar et al. [24]. A cylindrical bar with the same dimensions as in the 2D case is considered and, due to symmetry, only one eighth of the bar is modeled in the numerical simulation, see Figure 13. In order to trigger the necking, we also reduce the radius of the bar in the center of the specimen to 0.982 of the top radius. We used two meshes of $4 \times 4 \times 10$ and $8 \times 8 \times 20$ elements with refinement near the necking area (see Figure 13), and the loading is imposed as a vertical displacement on the top surface up to 9mm. Note here that other authors imposed a displacement of 7mm only. The maximum imposed displacement was increased here in order to fully distinguish results between $\bar{\text{F}}$ and non-$\bar{\text{F}}$ cases as will be seen subsequently.

We investigate for this example the behavior of the linearized operator described previously. We see in Table 2 the evolution of the relative Euclidian norm of the residual over the iterations for the Newton step corresponding to an imposed displacement of 7mm for the coarse mesh with Q2, Q3, $\bar{\text{F}}$ Q2/Q1 and $\bar{\text{F}}$ Q3/Q2. We can observe that convergence is slightly better for $\bar{\text{F}}$ cases when compared with the non-$\bar{\text{F}}$ cases.

In Figures 14 and 15, we plot for the coarse mesh the σ_{zz} component of the Cauchy stress tensor and the equivalent plastic strain on the deformed configuration for an imposed displacement of 7mm for quadratic and cubic NURBS with and without $\bar{\text{F}}$. Although results were computed on one eighth of the specimen, the results were reflected for better understanding. The scales are adapted for each case with different minimum and maximum values. Again we observe oscillation patterns for the non-$\bar{\text{F}}$ cases and smooth fields for the $\bar{\text{F}}$ cases when looking at the σ_{zz} component of the Cauchy stress tensor. Such oscillation patterns are not observed for the equivalent plastic strain but the minimum and maximum values obtained for Q2 are quite different from the three other cases.

In Figures 16 and 17 we plot the necking displacement and reaction force versus applied load for the coarse mesh. The results are shown for quadratic and cubic NURBS with and without $\bar{\text{F}}$ and for the reaction force we also plotted results obtained with the mixed finite element Q1/P0 extracted from Simo and Armero [7] for comparison. We can see that up to 6mm loading, the Q2 case produces a reasonable result. This is also the case for Q3 up to 7mm, which is the reason that motivated the increase of the maximum imposed displacement. When the load continues to increase, the solution becomes stiffer for the non-$\bar{\text{F}}$ cases and deviates from the reference one. We can see that both $\bar{\text{F}}$ cases are close to each other. A similar picture is observed when looking at the reaction force. However, we observe that Q3 is very close to Q2/Q1 up to the maximum load and that the difference between Q2/Q1 and Q3/Q2 is a little more pronounced than for the necking displacement. We can see that up to 6mm both $\bar{\text{F}}$ cases compare well with Q1/P0 that was obtained with a much finer mesh.

We plot similar results obtained with quadratic NURBS on the fine mesh in Figures 18 to 20. For the σ_{zz} component of the Cauchy stress tensor, we still observe oscillations for Q2 but not for Q2/Q1. Interestingly, although necking displacement and reaction force results are quite good for Q2 at 6mm with the fine mesh and close to Q3 results obtained on the coarse mesh, the stress oscillations produce minimum and maximum stress values that are very similar to Q2 on the coarse mesh. This indicates that although the mesh is finer, stress oscillations are not reduced with quadratic NURBS. Results obtained for the equivalent plastic strain are very similar to the ones obtained for the coarse mesh and Q3/Q2, although the maximum value for Q2/Q1 on the fine mesh is 10% higher. When looking at necking displacement and reaction force curves for Q2/Q1, we can see that up to 7mm the results are almost identical to Q3/Q2 on the coarse mesh. When the load increases further, the response is a little softer with the finer mesh, but the first mesh is probably too coarse in the necking area to capture the complete behavior at such a high loading.

Finally, we plot in Figures 21 and 22 the deformed meshes for an imposed displacement of 7mm and 9mm for $\bar{\text{F}}$ and non-$\bar{\text{F}}$ cubic NURBS with the coarse mesh and quadratic NURBS with the fine mesh. We can see for an imposed displacement of 7mm, as was observed on the necking displacement curves, that all cases shown are very similar. Although stress oscillations are present for the non $\bar{\text{F}}$ cases, the deformed configuration and meshes do not exhibit unusual behavior. For an imposed dis-

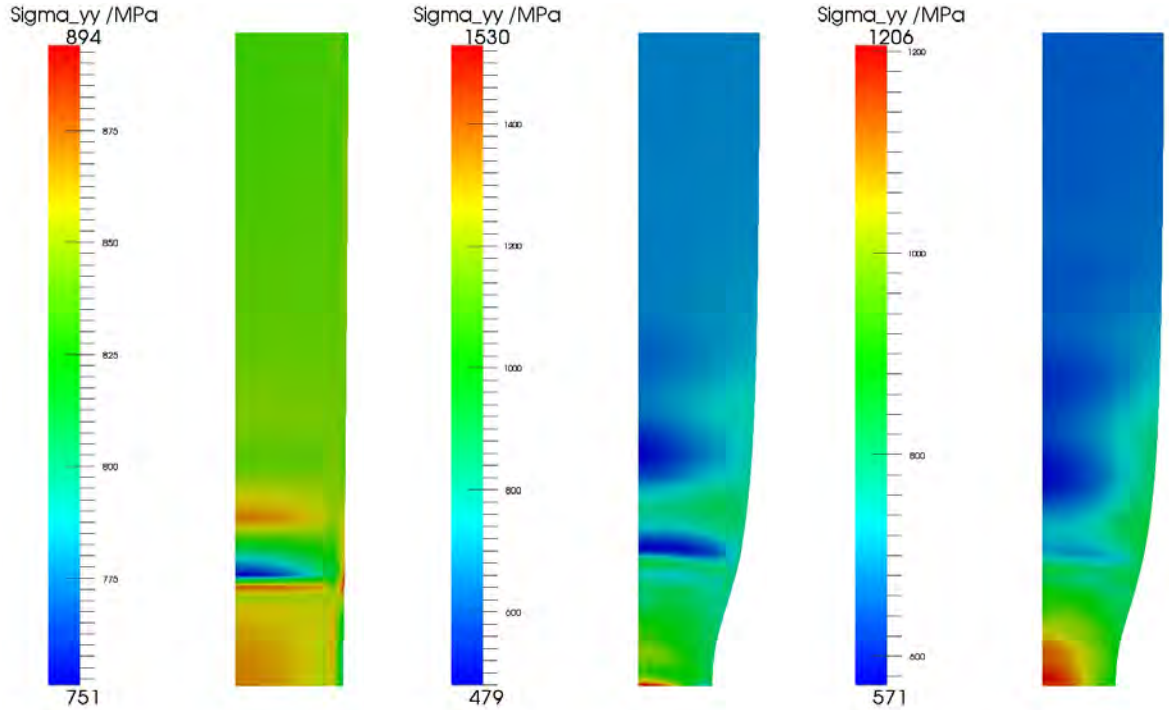

(a) (b) (c)

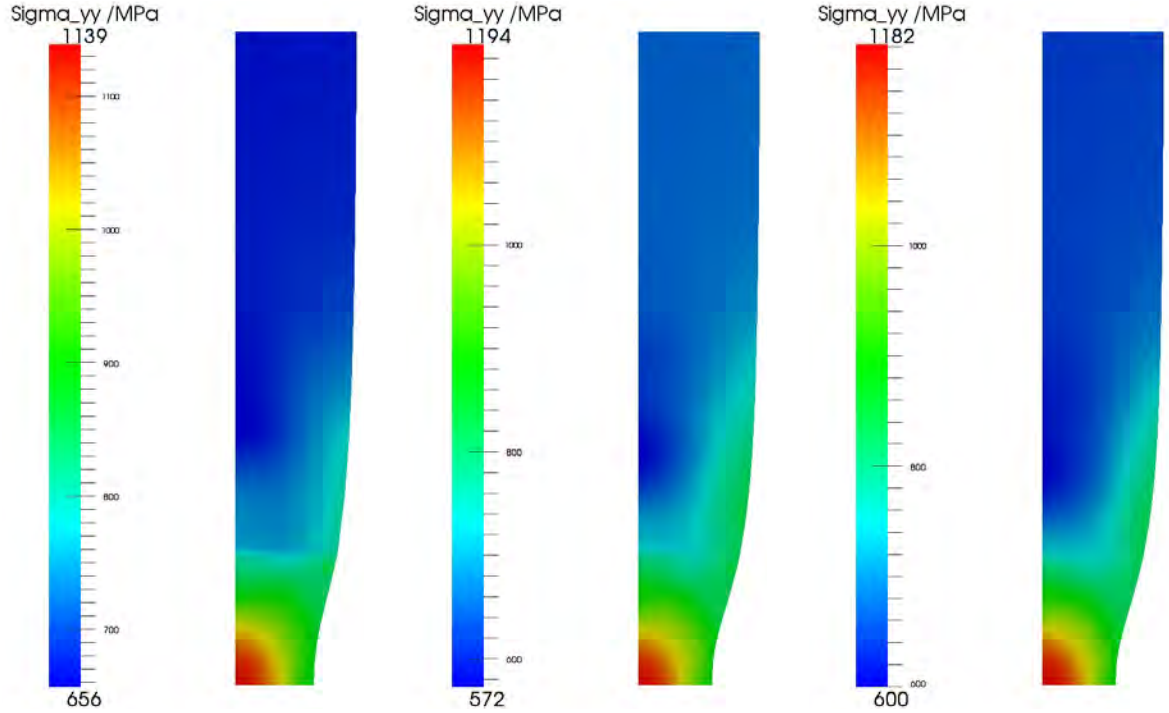

(d) (e) (f)

Figure 9: Plane strain necking, fine mesh with 200 elements. σ_{yy} Cauchy stress component for a vertical imposed displacement of 5mm for: (a) Q1, (b) Q2, (c) Q3, (d) $\bar{\mathrm{F}}$ Q1/Q0, (e) $\bar{\mathrm{F}}$ Q2/Q1, (f) $\bar{\mathrm{F}}$ Q3/Q2.

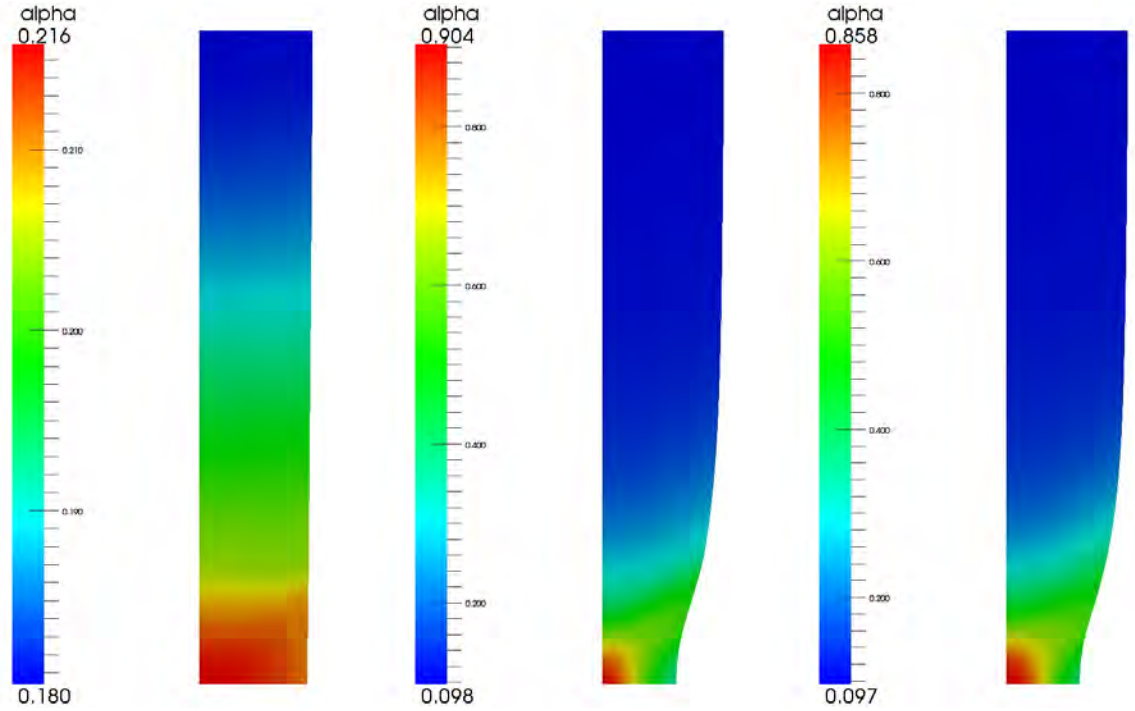

(a) (b) (c)

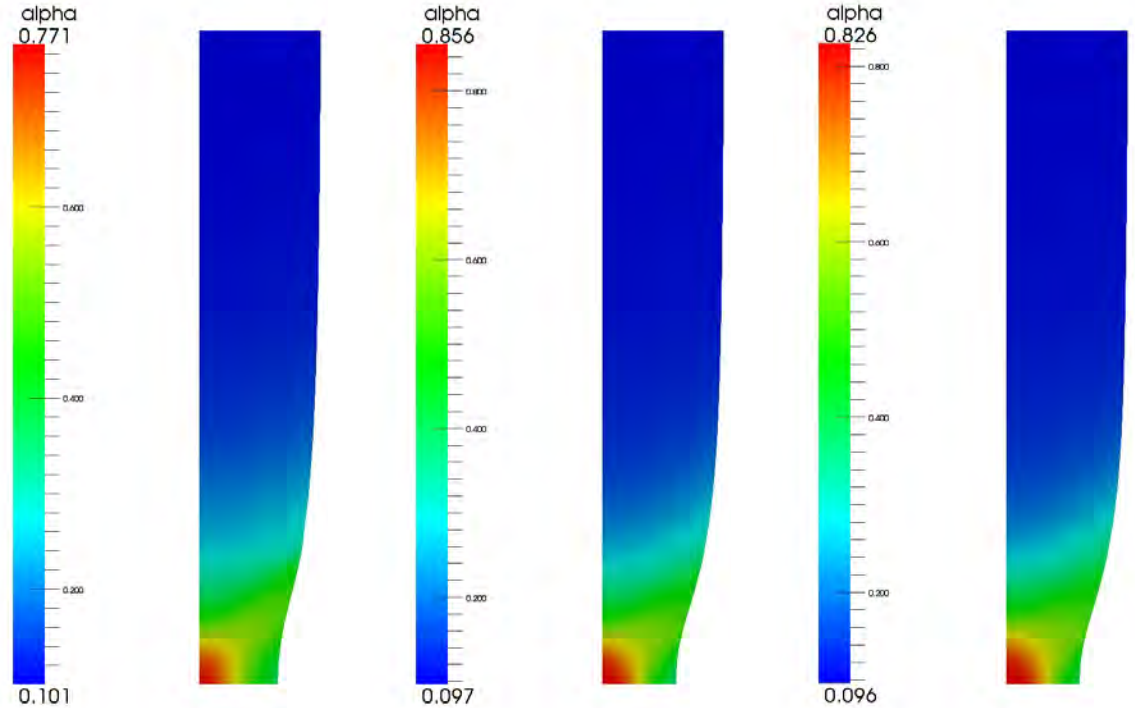

(d) (e) (f)

Figure 10: Plane strain necking, fine mesh with 200 elements. Equivalent plastic strain α for a vertical imposed displacement of 5mm for: (a) Q1, (b) Q2, (c) Q3, (d) $\bar{\mathrm{F}}$ Q1/Q0, (e) $\bar{\mathrm{F}}$ Q2/Q1, (f) $\bar{\mathrm{F}}$ Q3/Q2.

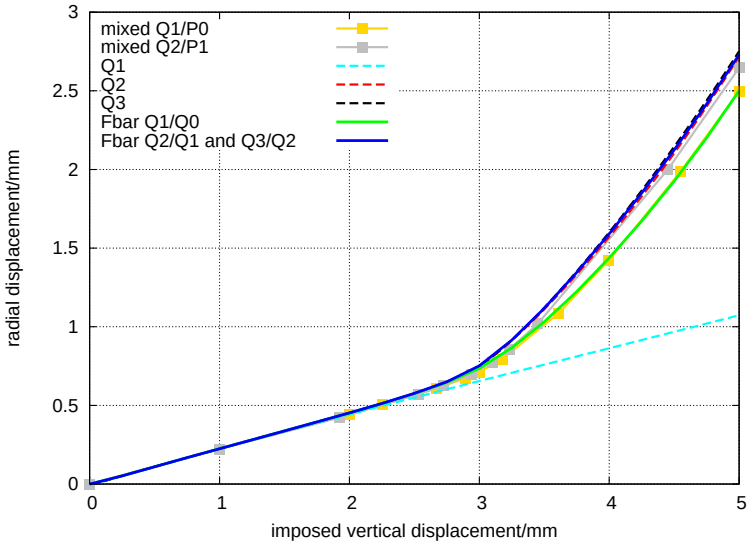

Figure 11: Plane strain necking, fine mesh with 200 elements. Necking displacement versus imposed displacement. Mixed finite elements are taken from Taylor [8].

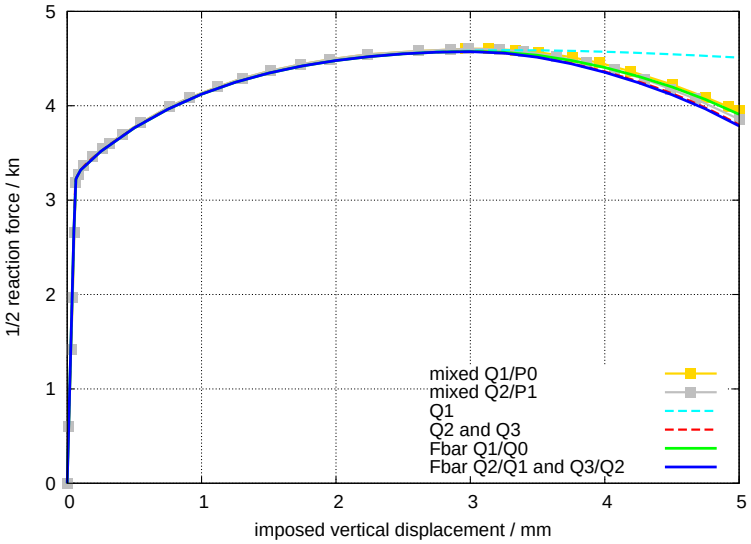

Figure 12: Plane strain necking, fine mesh with 200 elements. Half reaction force versus imposed displacement. Mixed finite elements are taken from Taylor [8].

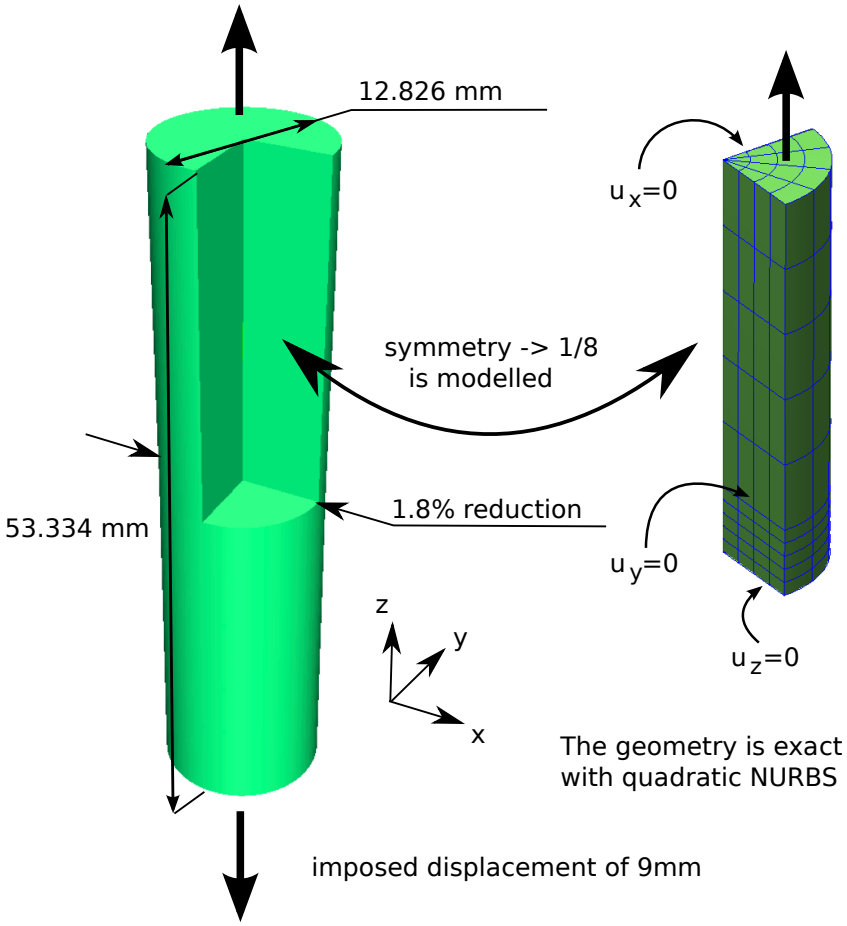

Figure 13: 3D necking: problem setup and mesh used for the computation

Iteration number	Relative norm of the residual			
	Q2	Q3	$\bar{F}$ Q2/Q1	$\bar{F}$ Q3/Q2
1	1.000000×10^{0}	1.000000×10^{0}	1.000000×10^{0}	1.000000×10^{0}
2	0.062626×10^{0}	0.0550812×10^{0}	0.064762×10^{0}	0.052881×10^{0}
3	0.952021×10^{-3}	0.0047900×10^{0}	0.777876×10^{-3}	0.562725×10^{-3}
4	0.621975×10^{-4}	0.335220×10^{-3}	0.130120×10^{-5}	0.955583×10^{-6}
5	0.865509×10^{-7}	0.467890×10^{-4}	0.246640×10^{-8}	0.183784×10^{-8}
6	0.129028×10^{-9}	0.756419×10^{-7}	0.171958×10^{-10}	0.229679×10^{-10}
7	0.307675×10^{-11}	0.593532×10^{-10}		

Table 2: 3D necking. Evolution of the relative norm of the residual during the Newton step with imposed displacement of 7mm for the coarse mesh with Q2, Q3, $\bar{F}$ Q2/Q1 and $\bar{F}$ Q3/Q2.

placement of 9mm, we can see that the deformation is too localized in the first layer of elements and that it is difficult to obtain an accurate solution. However, we can see, as was observed on the necking

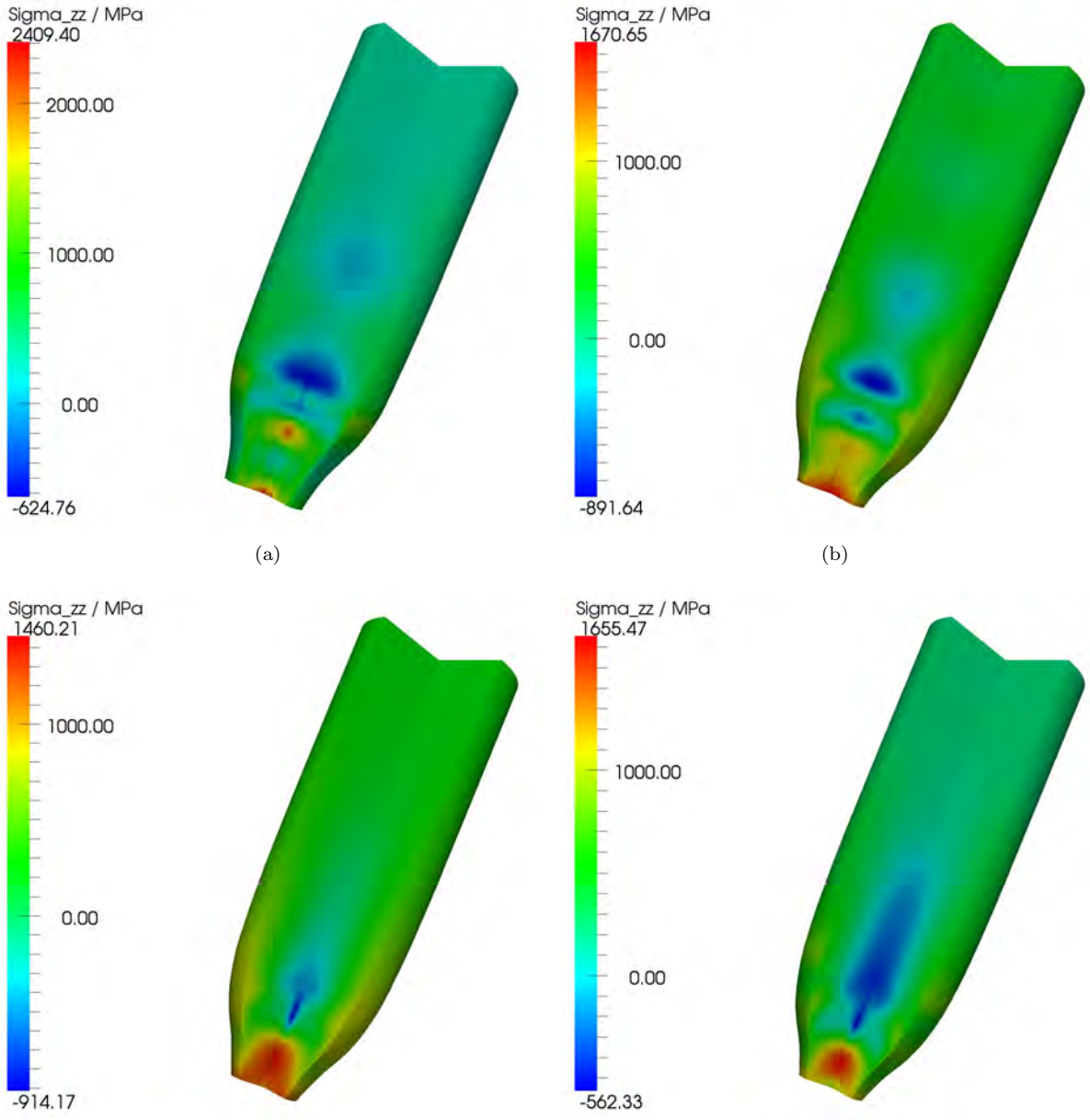

(a) (b)

(c) (d)

Figure 14: 3D necking, coarse mesh. σ_{zz} component of the Cauchy stress tensor on the deformed configuration for a vertical imposed displacement of 7mm. (a) Q2, (b) Q3, (c) $\bar{\mathrm{F}}$ Q2/Q1, (d) $\bar{\mathrm{F}}$ Q3/Q2.

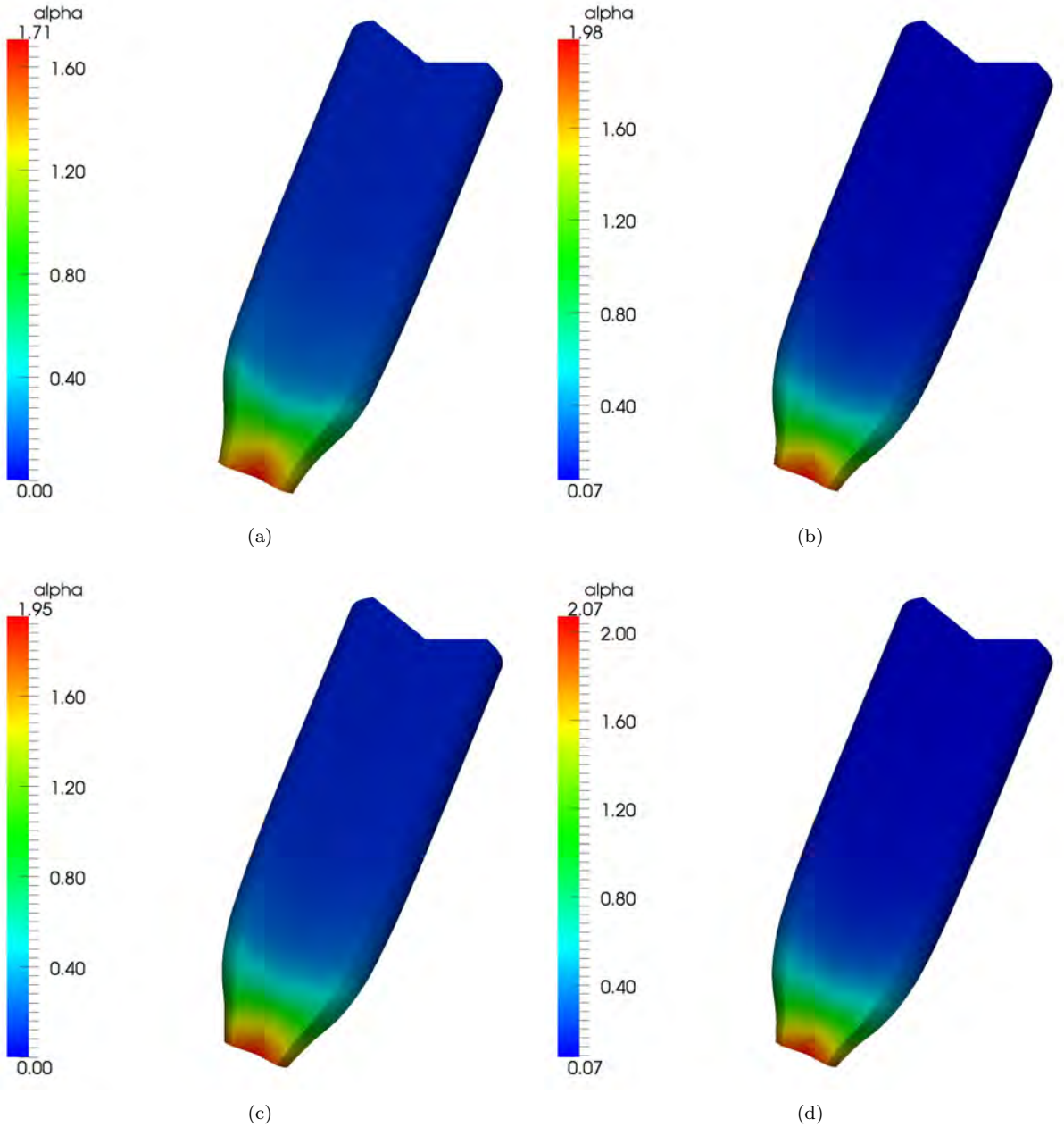

Figure 15: 3D necking, coarse mesh. Equivalent plastic strain α on the deformed configuration for a vertical imposed displacement of 7mm. (a) Q2, (b) Q3, (c) $\bar{\mathrm{F}}$ Q2/Q1, (d) $\bar{\mathrm{F}}$ Q3/Q2.

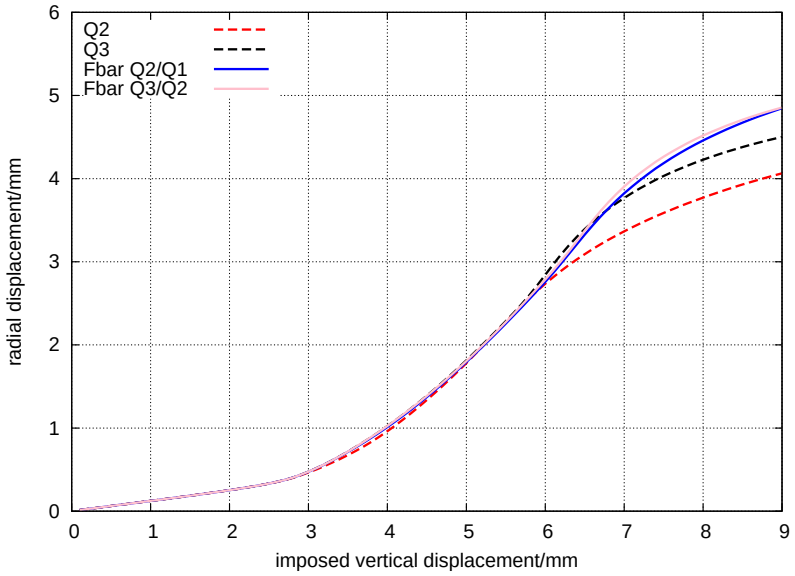

Figure 16: 3D necking, coarse mesh. Necking displacement versus imposed displacement.

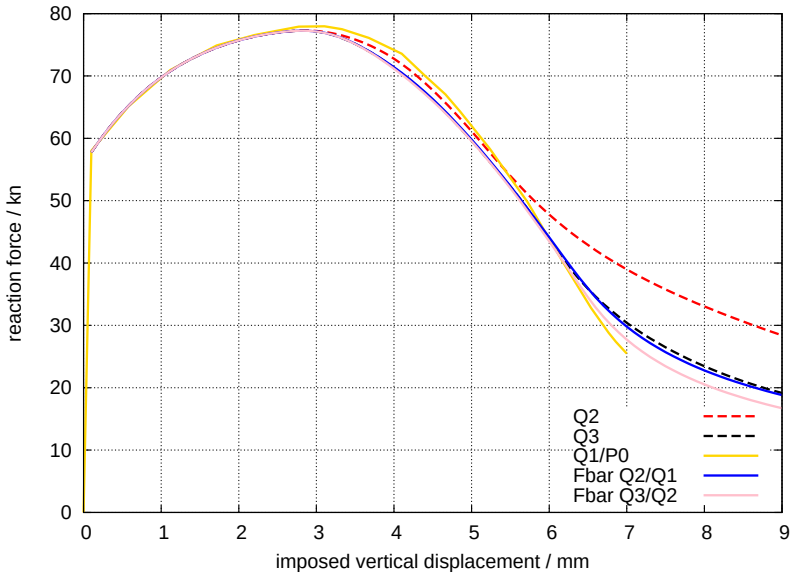

Figure 17: 3D necking, coarse mesh. Reaction force versus imposed displacement. Q1/P0 taken from Simo and Armero [7], for a calculation with six times as many elements as the present meshes.

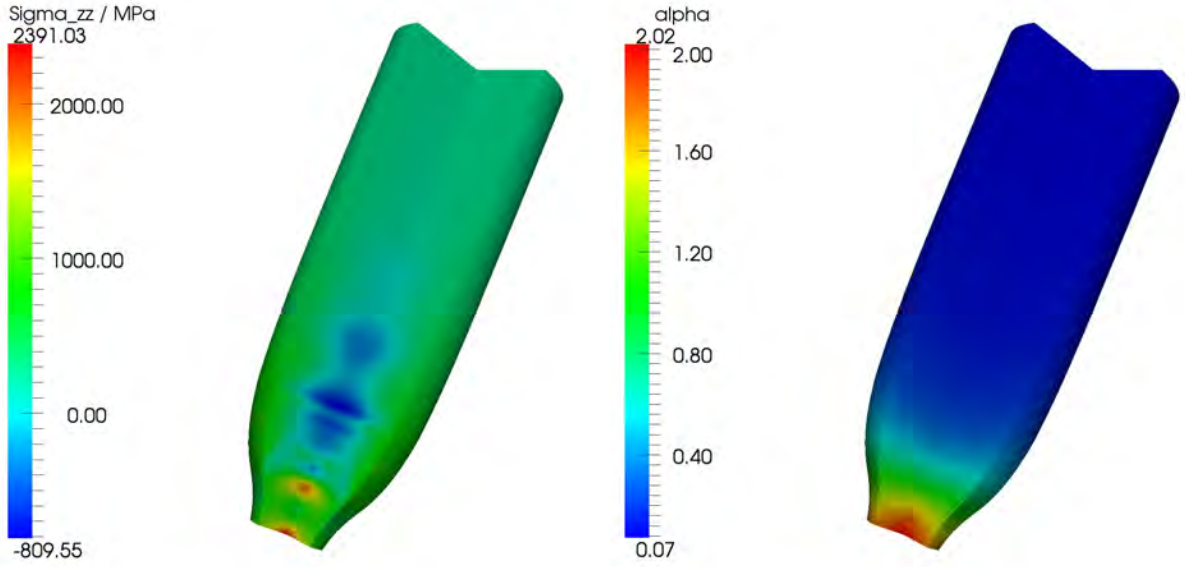

(a) (b)

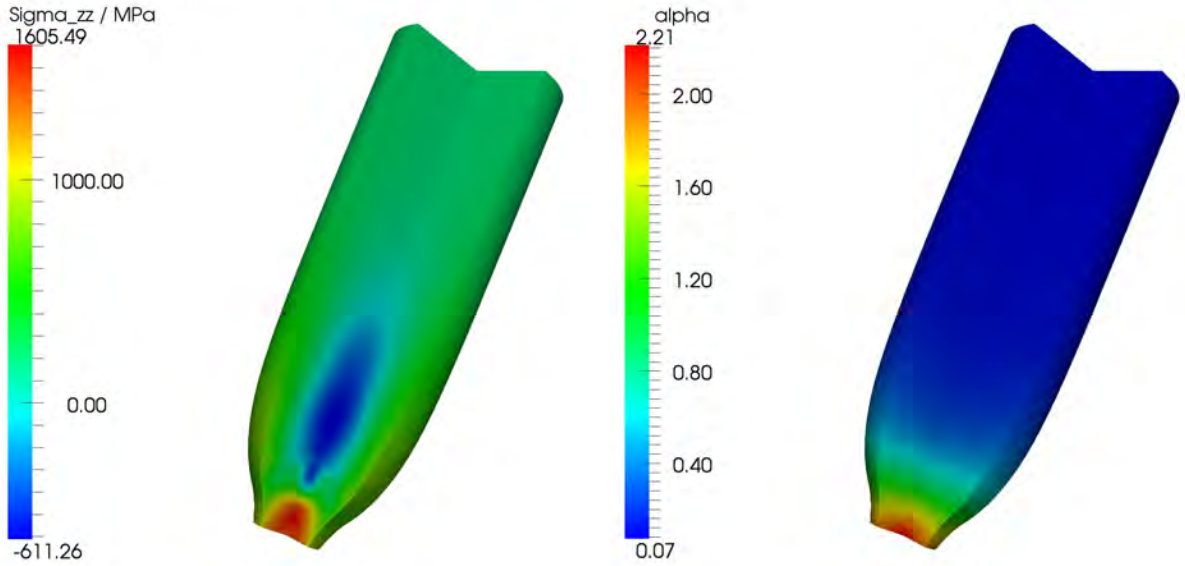

(c) (d)

Figure 18: 3D necking, fine mesh. σ_{zz} component of the Cauchy stress tensor and equivalent plastic strain α on the deformed configuration for a vertical imposed displacement of 7mm. (a) σ_{zz} Q2,(b) α Q2, (c) σ_{zz} $\bar{\mathrm{F}}$ Q2/Q1, (d) α $\bar{\mathrm{F}}$ Q2/Q1.

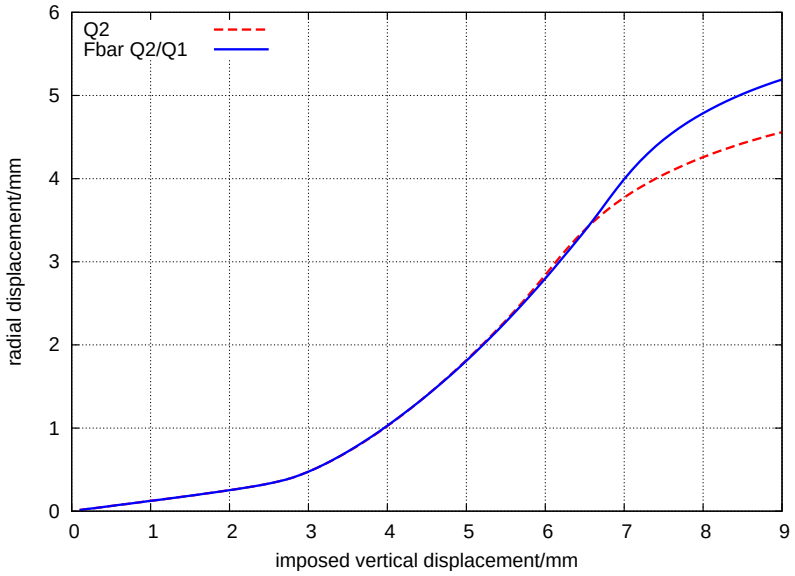

Figure 19: 3D necking, fine mesh. Necking displacement versus imposed displacement.

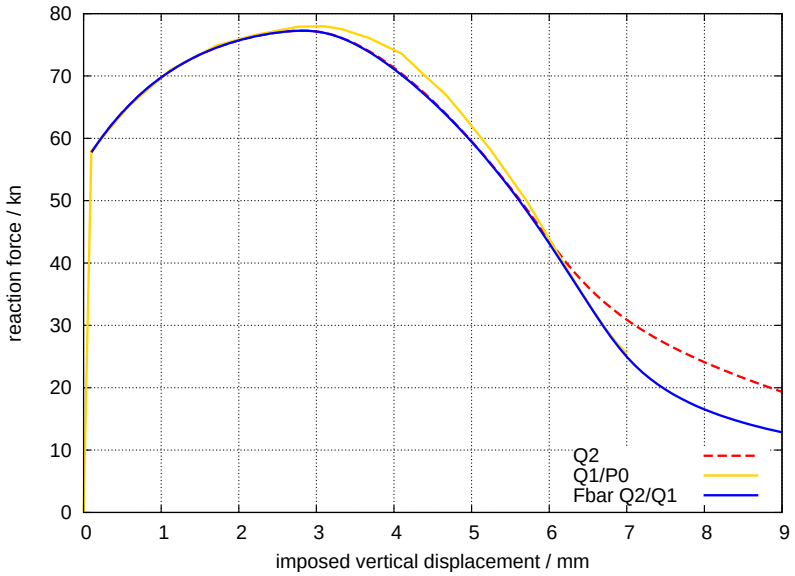

Figure 20: 3D necking, fine mesh. Reaction force versus imposed displacement. Q1/P0 taken from Simo and Armero [7]

displacement curves, that the non-$\bar{\mathrm{F}}$ cases do produce a stiffer response compared to the $\bar{\mathrm{F}}$ ones.

5. Conclusion

In this paper we have presented an evaluation of the performance of NURBS-based Isogeometric Analysis elements on problems of large-deformation elastoplasticity. The elastoplastic constitutive model utilizes the multiplicative splitting of the deformation gradient into elastic and plastic parts, $\mathbf{F} = \mathbf{F}^e\mathbf{F}^p$. The element technology is based on the $\bar{\mathrm{F}}$ method in which the dilatational component is projected on a lower-order space than the one used for the displacements. The $\bar{\mathrm{F}}$ method, which is derived from a modified minimum potential energy principle, is amenable to exact and explicit linearization, and produces a symmetric consistent tangent matrix. Normally, the reason to employ an $\bar{\mathrm{F}}$ approach is thought to be to circumvent mesh locking, which is manifest for the standard Q1 element. However, mesh locking is *not* the issue for higher-order elements in plasticity as our numerical results revealed. We studied the standard NURBS elements (*i.e.*, no $\bar{\mathrm{F}}$) Q1, Q2, Q3, and Q4, and compared them with the $\bar{\mathrm{F}}$ elements Q1/Q0, Q2/Q1, Q3/Q2, and Q4/Q3, and with the Q1/P0 element results of Simo and Armero [7], and the mixed elements of Taylor [8]. Our computations provided the following insights into the evaluation of higher-order NURBS elements in plasticity:

1. Point displacements are a misleading metric.
2. Graphs of reaction forces versus displacements may also be misleading.
3. Stress distributions, in the form of contour plots, expose the deficiencies of ill-conceived elements.
4. Mesh refinement studies are important indicators because results for ill-conceived elements are often no better for refined meshes than for coarse meshes.

In future work, we recommend performing serious mesh refinement studies to converge stress and equivalent plastic strains, as well as displacements and reaction forces. Of course, such studies will require significant computational resources and are easier said than done. Nevertheless, a database of results obtained would constitute an invaluable benchmarking tool and would eliminate some of the ambiguity in results that have appeared in the literature. The plane strain and 3D necking problems would seem appropriate for such an exercise. We feel the so-called Cooks membrane is not ideal for this purpose because the singularity at the reentrant corner dominates and clouds evaluation as emphasized to us by Kjell Magne Mathisen.

We believe our $\bar{\mathrm{F}}$ formulation utilizing the smooth NURBS spaces Qk/Qk-1 has been demonstrated herein to be an effective approach to solving large-deformation plasticity problems and has been shown to possess several attributes. However, it has some shortcomings concerning the structure of the consistent tangent stiffness matrix and numerical quadrature that should be addressed in future work. The tangent stiffness exhibits dense coupling on NURBS patches in the case of $k \geq 2$, due to the continuity of the $\bar{\mathrm{F}}$ jacobian determinant. In Elguedj et al. [1] we described an effective equation solution strategy for circumventing this coupling, but this strategy is not one that is currently supported in commercial finite element programs. Thus, it would be desirable to develop an equally effective generalization of the method that eliminated the coupling *ab initio*. We have employed Gauss quadrature rules of order $k+1$ in each coordinate direction on Bézier elements (see, *e.g.*, Scott et al. [25], Borden et al. [26]). This is necessary to attain full rank for Q1/Q0, but may amount to overkill for higher-order elements. It is always desirable to use quadrature rules with the minimum number of points in order to save computational effort. The challenge is to find minimum-point rules that maintain stability and do not otherwise degrade performance. Efforts to develop efficient quadrature rules for higher-order NURBS spaces were initiated in Hughes et al. [27]. Another direction that is appealing, due to its utter simplicity, is to use lower-order "reduced quadrature". In some academic circles this is considered anathema, but the fact remains it is successfully employed in widely used commercial finite element programs and, in our opinion, is certainly worth exploring. Benson et al. [28] have reported initial success with this approach.

Acknowledgements

T. Elguedj was partially supported through the J. Tinsley Oden Faculty Fellowship Research Program at the Institute for Computational Engineering and Sciences. T.J.R. Hughes was partially supported by the Office of Naval Research under Contract No. N00014-08-0992 and by the National Science Foundation under Grant No. 0700204. This support is

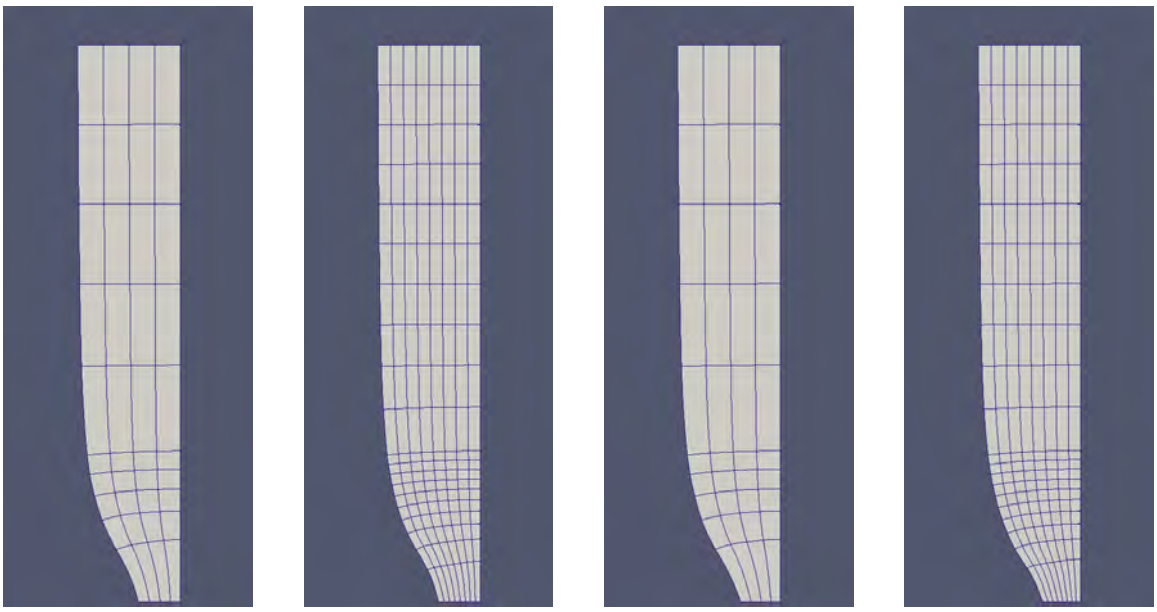

(a) (b) (c) (d)

Figure 21: 3D necking, deformed meshes at u=7mm. (a) Q3 coarse mesh, (b) Q2 fine mesh, (c) Q3/Q2 coarse mesh, (d) Q2/Q1 fine mesh.

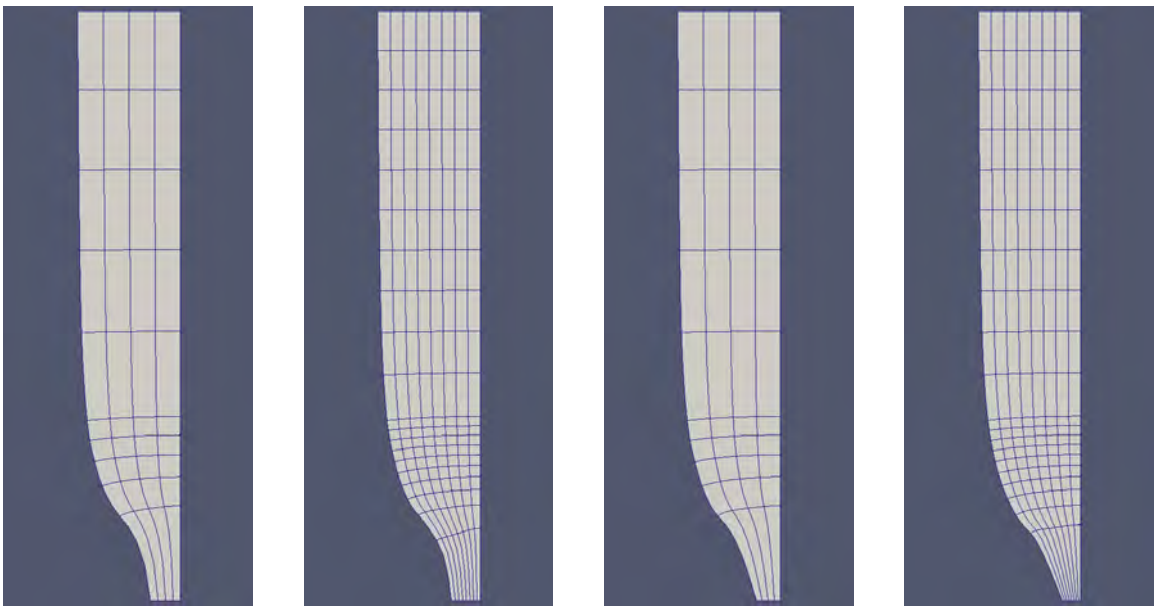

(a) (b) (c) (d)

Figure 22: 3D necking, deformed meshes at u=9mm. (a) Q3 coarse mesh, (b) Q2 fine mesh, (c) Q3/Q2 coarse mesh, (d) Q2/Q1 fine mesh.

gratefully acknowledged. The authors would like to thank Robert L. Taylor for providing results using mixed elements for the 2D necking and for fruitful discussions on the topics of the paper. We would also like to thank Kjell Magne Mathisen for helpful remarks on a rough draft of this paper.

A. Consistent elastoplastic tangent moduli

The algorithm given in Box 1 is amenable to exact linearization leading to a closed form expression for the consistent algorithmic tangent moduli in the finite strain range. The linearization can be carried out in closed form because of the hyperelastic nature of the stress response. The complete derivation can be found in Simo [13, 14], the equations are summarized in Box 2.

B. Consistency condition

Although the counterpart of the consistency condition can be determined in closed form for the case of linear hardening, it requires an iterative algorithm for the general non-linear case considered in this paper. The consistency condition is given in Eq. (17). For the nonlinear hardening law we have considered, its counterpart is written as:

$$\hat{f}(\Delta\gamma) = \|\mathbf{s}_{n+1}^{trial}\| - \sqrt{\frac{2}{3}}K(\alpha_n + \sqrt{\frac{2}{3}}\Delta\gamma) - 2\bar{\mu}\Delta\gamma = 0. \tag{27}$$

This expression furnishes a nonlinear equation for $\Delta\gamma$ which is easily solved using an iterative method. If the derivative of $k(\alpha)$ is easily computed in closed form, a Newton iteration scheme can be employed (see Simo and Hughes [4], Simo [14], Simo and Taylor [29]). The algorithm is given in Box 3 and is guaranteed to converge at a quadratic rate provided that $-k(\alpha)$ is convex, which is the case for the model given in Eq. (18).

References

[1] T. Elguedj, Y. Bazilevs, V. M. Calo, T. J. R. Hughes, B-bar and F-bar projection methods for nearly incompressible linear and non-linear elasticity and plasticity based on higher-order NURBS elements, Computer Methods in Applied Mechanics and Engineering 197 (2008) 2732–2762.

[2] T. J. R. Hughes, The Finite Element Method: Linear Static and Dynamic Finite Element Analysis, Dover Publications, Mineola NY, 2000.

[3] T. J. R. Hughes, Generalization of selective integration procedure to anisotropic and nonlinear media, International Journal for Numerical Methods in Engineering 15 (1980) 1413–1418.

[4] J. C. Simo, T. J. R. Hughes, Computational Inelasticity, Springer-Verlag, New York, 1998.

[5] T. J. R. Hughes, J. A. Cottrell, Y. Bazilevs, Isogeometric analysis: CAD, finite elements, NURBS, exact geometry and mesh refinement, Computer Methods in Applied Mechanics and Engineering 194 (2005) 4135–4195.

[6] J. A. Cottrell, T. J. R. Hughes, Y. Bazilevs, Isogeometric Analysis: Toward Integration of CAD and FEA, Wiley, 2009.

[7] J. C. Simo, F. Armero, Geometrically non-linear enhanced strain mixed methods and the method of incompatible modes, International Journal for Numerical Methods in Engineering 33 (1992) 1413–1449.

[8] R. L. Taylor, Isogeometric analysis of nearly incompressible solids, International Journal for Numerical Methods in Engineering 87 (1-5) (2010) 273–288.

[9] E. Cohen, R. Riesenfeld, G. Elber, Geometric Modeling with Splines: An Introduction, A.K. Peters Ltd., Wellesley, Massachusetts, 2001.

[10] L. Piegl, W. Tiller, The NURBS Book (Monographs in Visual Communication), Springer-Verlag, New York, 2nd edn., 1997.

[11] G. E. Farin, NURBS Curves and Surfaces: from Projective Geometry to Practical Use, A.K. Peters Ltd., Natick, MA, 1995.

[12] D. F. Rogers, An Introduction to NURBS With Historical Perspective, Academic Press, San Diego, CA, 2001.

[13] J. C. Simo, A framework for finite strain elastoplasticity based on maximum plastic dissipation and the multiplicative decomposition. Part I: continuum formulation, Computer Methods in Applied Mechanics and Engineering 66 (1988) 199–219.

[14] J. C. Simo, A framework for finite strain elastoplasticity based on maximum plastic dissipation and the multiplicative decomposition. Part II: computational aspects, Computer Methods in Applied Mechanics and Engineering 68 (1988) 1–31.

[15] R. Flory, Thermodynamic Relations for Highly Elastic Materials, Transactions of the Farday Society 57 (1969) 829–838.

[16] T. J. R. Hughes, R. L. Taylor, J. L. Sackman, Finite Element Formulation and Solution of Contact-Impact Problems in Continuum Mechanics-III, SESM Report 75-3, Department of Civil Engineering, The University of California, Berkeley, 1975.

[17] J. C. Simo, R. L. Taylor, K. S. Pister, Variational and projection methods for the volume contraint in finite deformation elasto-plasticity, Computer Methods in Applied Mechanics and Engineering 51 (1985) 177–208.

[18] J. C. Simo, R. L. Taylor, Quasi-incompressible finite elasticity in principal stretches. Continuum basis and numerical algorithm., Computer Methods in Applied Mechanics and Engineering 85 (1991) 273–310.

[19] E. A. de Souza Neto, D. Peric, M. Dutko, D. R. J. Owen, Design of simple low order finite elements for large strain analysis of nearly incompressible solids, International Journal of Solids and Structures 33 (1996) 3277–3296.

[20] E. A. de Souza Neto, F. M. A. Pires, D. R. J. Owen, F-bar based linear triangles and tetrahedra for finite

1. Spatial elasticity tensor $\mathbf{C}$ for hyperelastic model

   $$\mathbf{C} = (JU')'J\mathbf{1}\otimes\mathbf{1} - 2JU'\mathcal{I} + \bar{\mathbf{C}}$$

   with $\bar{\mathbf{C}} = 2\bar{\mu}[\mathbf{I} - \frac{1}{3}\mathbf{1}\otimes\mathbf{1}] - \frac{2}{3}[\boldsymbol{s}\otimes\mathbf{1} + \mathbf{1}\otimes\boldsymbol{s}]$

2. Scaling factors

   $$\beta_0 = 1 + \frac{k'}{3\bar{\mu}} \qquad \beta_1 = \frac{2\bar{\mu}\Delta\gamma}{\|\boldsymbol{s}_{n+1}^{trial}\|}$$
   $$\beta_2 = \left[1 - \frac{1}{\beta_0}\right]\frac{2}{3}\frac{\|\boldsymbol{s}_{n+1}^{trial}\|}{\bar{\mu}}\Delta\gamma$$
   $$\beta_3 = \frac{1}{\beta_0} - \beta_1 + \beta_2 \qquad \beta_4 = \left[\frac{1}{\beta_0} - \beta_1\right]\frac{\|\boldsymbol{s}_{n+1}^{trial}\|}{\bar{\mu}}$$

3. Consistent moduli

   $$\mathbf{C}_{n+1}^{ep} = \mathbf{C}_{n+1}^{trial} - \beta_1\bar{\mathbf{C}}_{n+1}^{trial} - 2\bar{\mu}\beta_3\boldsymbol{n}\otimes\boldsymbol{n} - 2\bar{\mu}\beta_4\mathrm{sym}\left[\boldsymbol{n}\otimes\mathrm{dev}[\boldsymbol{n}^2]\right]$$

Box 2: Consistent elastoplastic moduli for the radial return algorithm given in Box 1.

strain analysis of nearly incompressible solids. Part I: formulation and benchmarking, International Journal for Numerical Methods in Engineering 62 (2005) 353–383.

[21] F. Armero, S. Glaser, On the formulation of enhanced strain finite elements in finite deformation, Engineering Computations 14 (1997) 759–791.

[22] B. Ramesh, A. Maniatty, Stabilized finite element formulation for elastic-plastic finite deformations, Computer Methods in Applied Mechanics and Engineering 194 (2005) 775–800.

[23] E. N. Dvorkin, A. P. Assanelli, Implementation and stability analysis of the QMITC-TLH elasto-plastic finite strain (2D) element formulation, Computers and Structures 75 (2000) 305–312.

[24] C. A. de Saracibar, M. Chiumenti, Q. Valverde, M. Cervera, On the orthogonal subgrid scale pressure stabilization of finite deformation J2 plasticity, Computer Methods in Applied Mechanics and Engineering 195 (2006) 1224–1251.

[25] M. A. Scott, M. J. Borden, C. V. Verhoosel, T. W. Sederberg, T. J. R. Hughes, Isogeometric finite element data structures based on Bézier extraction of T-splines, International Journal for Numerical Methods in Engineering 88 (2011) 126–156.

[26] M. J. Borden, M. A. Scott, J. A. Evans, T. J. R. Hughes, Isogeometric finite element data structures based on Bézier extraction of NURBS, International Journal for Numerical Methods in Engineering 87 (2011) 15–47.

[27] T. J. R. Hughes, A. Reali, G. Sangalli, Efficient quadrature for NURBS-based isogeometric analysis, Computer Methods in Applied Mechanics and Engineering doi:10.1016/j.cma.2008.12.004.

[28] D. J. Benson, Y. Bazilevs, M. C. Hsu, T. J. R. Hughes, A large deformation, rotation-free, isogeometric shell, Computer Methods in Applied Mechanics and Engineering 200 (2011) 1367–1378.

[29] J. C. Simo, R. L. Taylor, Consistent tangent operators for rate independent elastoplasticity, Computer Methods in Applied Mechanics and Engineering 48 (1985) 101–118.

1. Initialize

$$\Delta\gamma^{(0)} = 0$$

2. Iterate
   WHILE $|\hat{f}(\Delta\gamma^{(i)})| < 0$, DO $i = i + 1$

   Compute iterate $\Delta\gamma^{(i+1)}$

$$\hat{f}(\Delta\gamma^{(i)}) = \|\mathbf{s}_{n+1}^{trial}\| - \sqrt{\frac{2}{3}}k(\alpha_n + \sqrt{\frac{2}{3}}\Delta\gamma^{(i)}) - 2\bar{\mu}\Delta\gamma^{(i)}$$

$$\hat{f}'(\Delta\gamma^{(i)}) = -2\bar{\mu}\left[1 + \frac{k'(\alpha_n + \sqrt{\frac{2}{3}}\Delta\gamma^{(i)})}{3\bar{\mu}}\right]$$

$$\Delta\gamma^{(i+1)} = \Delta\gamma^{(i)} - \frac{\hat{f}(\Delta\gamma^{(i)})}{\hat{f}'(\Delta\gamma^{(i)})}$$

3. Update equivalent plastic strain

$$\alpha_{n+1} = \alpha_n + \sqrt{\frac{2}{3}}\Delta\gamma^{(i+1)}$$

Box 3: Iterative procedure for solving the counterpart of the consistency condition.